MOX-Report No. 81/2020

Stability analysis of polytopic Discontinuous Galerkin approximations of the Stokes problem with applications to fluid-structure interaction problems

Antonietti, P. F.; Mascotto, L.; Verani, M.; Zonca, S.

MOX, Dipartimento di Matematica
Politecnico di Milano, Via Bonardi 9 - 20133 Milano (Italy)

mox-dmat@polimi.it http://mox.polimi.it

Stability analysis of polytopic Discontinuous Galerkin approximations of the Stokes problem with applications to fluid-structure interaction problems

Paola F. Antonietti[♯] and Lorenzo Mascotto[♭] and Marco Verani[♯] and Stefano Zonca[♯]

December 2, 2020

[♯] MOX – Modelling and Scientific Computing
Dipartimento di Matematica, Politecnico di Milano
Piazza Leonardo da Vinci, 20133 Milano, Italy
paola.antonietti@polimi.it
marco.verani@polimi.it
stefano.zonca@polimi.it

[♭] Fakultät für Mathematik, Universität Wien, Austria
lorenzo.mascotto@univie.ac.at

Keywords: discontinuous Galerkin; polytopic meshes; fluid-structure interaction.

Abstract

We present a stability analysis of the Discontinuous Galerkin method on polygonal and polyhedral meshes (PolyDG) for the Stokes problem. In particular, we analyze the discrete *inf-sup* condition for different choices of the polynomial approximation order of the velocity and pressure approximation spaces. To this aim, we employ a generalized *inf-sup* condition with a pressure stabilization term. We also prove a priori *hp*-version error estimates in suitable norms. We numerically check the behaviour of the *inf-sup* constant and the order of convergence with respect to the mesh configuration, the mesh-size, and the polynomial degree. Finally, as a relevant application of our analysis, we consider the PolyDG approximation for a fluid-structure interaction problem and we numerically explore the stability properties of the method.

1 Introduction

It is well known that a crucial aspect involving the stability of the numerical scheme associated with the Stokes problem is the *inf-sup* condition that establishes a constraint in the choice of the velocity and pressure discrete spaces; see, e.g, [19, 13]. This aspect, in the context of polygonal methods, is still under investigation and only few results are present in the literature; see, e.g., [26, 29, 12, 28].

The Discontinuous Galerkin (DG) method handles meshes with elements of general shape and has proved to be suited for the approximation of fluid and structure models, possibly involving moving domains, see, e.g. [32, 54]. The discrete *inf-sup* condition for DG methods has been analyzed in the following works. In [26], the Local DG method for the Stokes problem is formulated in a conservative way, by introducing the stress as unknown. Here, meshes with hanging nodes and elements of different shape are considered, provided that they are affinely-equivalent to an element of a fixed set of reference elements. Moreover, an *inf-sup* condition and optimal order estimates are proven, when the pair of polynomials of degree k and $k-1$ is chosen for the velocity and pressure spaces. However, the formulation requires a stability term for both the velocity and the pressure. In [49], the *inf-sup* condition is proven for a pressure stabilized formulation on hexahedral meshes allowing hanging nodes, when the pair $\mathbb{Q}_k - \mathbb{Q}_k$ is chosen. In [29, 30], the authors show the *inf-sup* condition for equal-order approximation $\mathbb{P}_k$ for both the velocity and pressure in the case of a pressure stabilized formulation on meshes consisting of elements of various shape, provided that each element is affinely-equivalent to one in a fixed set of reference elements, and admitting hanging nodes. In [48], the authors propose a mixed DG formulation without pressure stabilization for the Stokes problem and show a priori error estimates. The *inf-sup* condition is proven for the pair of spaces $\mathbb{Q}_k - \mathbb{Q}_{k-1}$ on tensor product meshes, possibly with hanging nodes. In [58], the *inf-sup* condition is proven for the pairs of spaces $\mathbb{Q}_k - \mathbb{Q}_{k-1}$ and $\mathbb{Q}_k - \mathbb{Q}_{k-2}$ without any pressure stabilization on quadrilateral and hexahedral meshes with hanging nodes; see also [52, 47, 59]. Numerical tests showing the dependence of the *inf-sup* constants are performed for the pairs of spaces $\mathbb{Q}_k - \mathbb{Q}_{k'}$, with $k' = k, k-1, k-2$. In [41], the *inf-sup* condition is proven on triangular and tetrahedral meshes without any pressure stabilization term for the pair of spaces $\mathbb{P}_k - \mathbb{P}_{k-1}$ employing the Brezzi-Douglas-Marini spaces. In [37], the pair of spaces $\mathbb{P}_k - \mathbb{P}_{k-1}$ with the Crouzeix-Raviart elements is used to prove the *inf-sup* condition on triangular meshes.

In this work, we consider the Discontinuous Galerkin method on polygonal and polyhedral grids (PolyDG) that extends the standard DG method to polytopic meshes; see, e.g., [10, 5, 60, 25, 3, 23, 6, 4]. In this framework, we study the discrete stability and well-posedness for the Stokes problem, by presenting an analysis that covers at once the two- and three- dimensional cases. Under suitable assumptions, we prove that the *inf-sup* constant is independent of the mesh size. Notwithstanding, it is not robust with respect to the polynomial degree and this restriction propagates to the convergence analysis, with a deterioration of the convergence in terms of the polynomial degree. However, we provide numerical evidence that the discrete *inf-sup* constant has a much milder dependence

on the polynomial degree in practice. Moreover, the mesh assumptions seem to be too restrictive and, in fact, the method results to be *inf-sup* stable also for pathological configurations. In the two-dimensional case, we numerically assess the robustness of the *inf-sup* constant with respect to the mesh size and the polynomial degree for different types of mesh elements, including elements with degenerating edges, and we numerically estimate the order of convergence to the mesh size and the polynomial degree.

Besides, with the aim of further exploring the relevance of our stability analysis, we consider a fluid-structure interaction (FSI) problem where both the Stokes and the elastodynamics equations are solved based on employing the PolyDG method. In fact, it is well known that the study of FSI problems is of paramount importance in many engineering and biomedical applications; see, e.g., [43, 17, 61, 56, 36, 46], where a fluid, for instance modeled via the Stokes equations, interacts with a structure, modeled via the elastodynamics equations. In particular, a special class of FSI applications that requires a lot of effort from the numerical viewpoint arises under the large deformations condition occurring in time-dependent processes. Indeed, to correctly model such problems, ad-hoc techniques are mandatory to deal with the movement of the structures. A classical strategy to overcome this issue is the employment of the Arbitrary Lagrangian Eulerian (ALE) approach. It consists in deforming the fluid grid according to the structure displacement, yet maintaining a "honouring" mesh at the fluid-structure interface and generating an arbitrary deformation of the elements in the interior of the fluid mesh; see, e.g., [31, 42, 55]. Another way that preserves the alignment of the fluid and structure grids at the interface is to use approaches based on remeshing and mesh-adaptation techniques; see, e.g., [57, 16]. A different category of approaches are based on employing unfitted meshes that allow to keep the fluid grid fixed in time, while the structure mesh is free to move; see, e.g., [38, 45, 62, 35, 39, 15, 44, 27, 2, 14, 34, 1, 20]. Often, this requires the handling of polygonal and polyhedral elements appearing in the fluid mesh, e.g., due to the intersection between the fluid and structure elements, and in the solid mesh, e.g., due to the presence of hanging nodes; see, e.g., [7, 11]. For this kind of approaches, it is mandatory that the underlining discretization methods can robustly and efficiently support meshes made of arbitrarily shaped elements. In this respect, a deep understanding of the stability properties of the numerical scheme with respect to possibly pathological meshes is of crucial importance.

The paper is organized as follows. Section 2 introduces the transient Stokes problem and its PolyDG approximation. In Section 3, we prove the well-posedness of the PolyDG approximation of the (stationary) Stokes problem, with a particular emphasis to the discrete *inf-sup* condition. In particular, in Section 4 we estimate the discrete *inf-sup* constant and numerically evaluate it for different choices of the discrete velocity and pressure spaces and for different grids. Section 5 is devoted to the proof of a priori error estimates of the Stokes problem. In Section 6, we introduce a fluid-structure interaction problem and we present its fully-discrete PolyDG approximation. In Section 7 we show some numerical results for the Stokes and FSI problems. Finally, in Section 8, we draw some conclusions.

In the sequel, the notation $\lesssim$ and $\gtrsim$ means that the inequalities are valid up to multiplicative constants that are independent of the discretization parameters, but might depend on the physical parameters of the underlying problem.

2 The transient Stokes problem

Having in mind the PolyDG discretization of FSI problems as a reference application, in this section we consider the transient Stokes problem which reads as follows: given a final time $T > 0$ and $\boldsymbol{f}$ a (regular) forcing term, find the velocity $\boldsymbol{u} = \boldsymbol{u}(t)$ and the pressure $p = p(t)$ such that, for all $t \in (0, T]$,

$$\rho \partial_t \boldsymbol{u} - \mu \Delta \boldsymbol{u} + \nabla p = \boldsymbol{f} \qquad \text{in } \Omega, \tag{1a}$$

$$\nabla \cdot \boldsymbol{u} = 0 \qquad \text{in } \Omega, \tag{1b}$$

$$\boldsymbol{u} = 0 \qquad \text{on } \partial\Omega. \tag{1c}$$

Problem (1) is supplemented with sufficiently regular initial conditions $\boldsymbol{u}(\boldsymbol{x}, 0) = \boldsymbol{u}^0(\boldsymbol{x})$ in Ω. To guarantee the well-posedness of the problem, we prescribe that $p \in L^2_0(\Omega)$, where $L^2_0(\Omega)$ is the space of $L^2(\Omega)$ functions with zero average over Ω.

We introduce the functional spaces

$$\boldsymbol{V} = \{\boldsymbol{v} \in [H^1(\Omega)]^d, d = 2, 3, \text{ such that } \boldsymbol{v}|_{\partial\Omega} = 0\}$$

and $Q = L^2_0(\Omega)$ and endow them with the norms

$$\|\boldsymbol{v}\|_{\boldsymbol{V}} := \|\mu^{\frac{1}{2}} \nabla \boldsymbol{v}\|_{L^2(\Omega)} \quad \text{and} \quad \|q\|_Q := \|q\|_{L^2(\Omega)}.$$

The weak formulation of problem (1) reads as follows: find $(\boldsymbol{u}, p) \in \boldsymbol{V} \times Q$, such that, for all $t \in (0, T]$,

$$(\rho \partial_t \boldsymbol{u}, \boldsymbol{v})_\Omega + a(\boldsymbol{u}, \boldsymbol{v}) + b(p, \boldsymbol{v}) - b(q, \boldsymbol{u}) = (\boldsymbol{f}, \boldsymbol{v})_\Omega \quad \forall (\boldsymbol{v}, q) \in \boldsymbol{V} \times Q, \tag{2}$$

where

$$a : \boldsymbol{V} \times \boldsymbol{V} \to \mathbb{R}, \quad a(\boldsymbol{u}, \boldsymbol{v}) = \int_\Omega \mu \nabla \boldsymbol{u} : \nabla \boldsymbol{v},$$

$$b : Q \times \boldsymbol{V} \to \mathbb{R}, \quad b(p, \boldsymbol{v}) = -\int_\Omega p \nabla \cdot \boldsymbol{v},$$

and $(\cdot, \cdot)_\Omega$ denotes the L^2-inner product over the domain Ω.

It is well-known that the bilinear form $b(\cdot, \cdot)$ satisfies a continuous *inf-sup* condition; see, e.g., [13]. More precisely, there exists a universal positive constant depending only on Ω such that, to all $q \in L^2_0(\Omega)$, we associate a function $\boldsymbol{v}_q \in \boldsymbol{V}$ satisfying $\nabla \cdot \boldsymbol{v}_q = q$ and

$$\beta \|\boldsymbol{v}_q\|_{\boldsymbol{V}} \leq \|q\|_{L^2(\Omega)}. \tag{3}$$

2.1 PolyDG semi-discrete approximation of the transient Stokes problem

First, we introduce the necessary notation and key analytical results required for the definition and analysis of PolyDG semi-discrete approximation of the transient Stokes problem.

We introduce a mesh $\mathcal{T}_h$ composed of polytopic elements K of arbitrary shape. We indicate with h_K the diameter of the element K. We define an interface to be either the intersection of the $(d-1)$-dimensional facets of two neighboring elements or the intersection of the $(d-1)$-dimensional facets of an element with the boundary of Ω. When $d = 2$, interfaces coincide with faces and consist of line segments; when $d = 3$, we assume that each interface consists of a general planar polygon that we assume that can be further decomposed into a set of co-planar triangles, denoted as faces.

With this notation, we collect all the $(d-1)$-dimensional faces in the set $\mathcal{F}_h$, i.e., any face $F \in \mathcal{F}_h$ is always defined as a set of $(d-1)$-dimensional simplices (line segments or triangles); cf. [25, 24]. We also decompose the faces $\mathcal{F}_h$ into $\mathcal{F}_h = \mathcal{F}_h^i \cup \mathcal{F}_h^b$, where $\mathcal{F}_h^i$ denotes the set of interior faces and $\mathcal{F}_h^b$ denotes the set of boundary faces. To avoid technicalities, in the following we assume that ρ and μ are piecewise constant over the mesh.

For given integers $\ell, m \geq 1$, we introduce the DG finite element spaces

$$\mathbf{V}_h^\ell = \{\boldsymbol{v} \in [L^2(\Omega)]^d : \boldsymbol{v}|_K \in [\mathcal{P}^\ell(K)]^d \, \forall K \in \mathcal{T}_h\},$$
$$Q_h^m = \{q \in L_0^2(\Omega) : q|_K \in \mathcal{P}^m(K) \, \forall K \in \mathcal{T}_h\},$$

where $\mathcal{P}^k(K)$, $k \geq 1$, denotes the space of polynomials defined over the element $K \in \mathcal{T}_h$ of total degree at most k. In practice, the shape functions and the degrees of freedom are directly generated on the physical element $K \in \mathcal{T}_h$ with the "bounding box" technique; see, e.g., [25].

On any interior face $F \in \mathcal{F}_h^i$ and for sufficiently regular scalar, vector-valued and symmetric tensor-valued functions q, $\boldsymbol{v}$ and $\boldsymbol{T}$, respectively, we define the *average* and *jump* operators as

$$\{\boldsymbol{v}\} = \frac{1}{2}\left(\boldsymbol{v}^+ + \boldsymbol{v}^-\right), \qquad [\![q]\!] = q^+\boldsymbol{n}^+ + q^-\boldsymbol{n}^-,$$
$$\{\boldsymbol{T}\} = \frac{1}{2}\left(\boldsymbol{T}^+ + \boldsymbol{T}^-\right), \qquad [\![\boldsymbol{v}]\!] = \boldsymbol{v}^+ \odot \boldsymbol{n}^+ + \boldsymbol{v}^- \odot \boldsymbol{n}^-,$$

where $q^\pm$, $\boldsymbol{v}^\pm$ and $\boldsymbol{T}^\pm$ denote the traces of q, $\boldsymbol{v}$ and $\boldsymbol{T}$ on F taken within the interior of $K^\pm$ and where $\boldsymbol{v} \odot \boldsymbol{n} = (\boldsymbol{v}\boldsymbol{n}^T + \boldsymbol{n}\boldsymbol{v}^T)/2$. The jump $[\![\boldsymbol{v}]\!]$ is a symmetric tensor-valued function. On a boundary face $F \in \mathcal{F}_h^b$, we set analogously

$$\{\boldsymbol{v}\} = \boldsymbol{v}, \qquad [\![q]\!] = q\boldsymbol{n},$$
$$\{\boldsymbol{T}\} = \boldsymbol{T}, \qquad [\![\boldsymbol{v}]\!] = \boldsymbol{v} \odot \boldsymbol{n}.$$

We also introduce the L^2-inner products over a domain $Z \subset \mathbb{R}^d$, $d = 1, 2, 3$, and a face $F \in \mathcal{F}_h$ with the shorthand notation $(\cdot,\cdot)_Z$ and $(\cdot,\cdot)_F$, respectively.

Given $s > 1/2$, associated with any mesh $\mathcal{T}_h$, we introduce the broken Sobolev space

$$H^s(\mathcal{T}_h) := \left\{ v \in L^2(\Omega) \mid v|_K \in H^s(K) \text{ for all } K \in \mathcal{T}_h \right\}.$$

The standard Dirichlet trace operator is well defined on the skeleton of the mesh for functions in $H^s(\mathcal{T}_n)$.

Define the stabilization functions $\sigma_v \in L^\infty(\mathcal{F}_h)$ and $\sigma_p \in L^\infty(\mathcal{F}_h)$ as follows.

Definition 2.1 *We define the functions $\sigma_v : \mathcal{F}_h \to \mathbb{R}$ and $\sigma_p : \mathcal{F}_h^i \to \mathbb{R}$ as*

$$\sigma_v|_F = \begin{cases} \gamma_v \max\limits_{K^+,K^-} \left\{ \dfrac{\ell^2 \mu}{h_K} \right\} & F \in \mathcal{F}_h^i, \\ \gamma_v \dfrac{\ell^2 \mu}{h_K} & F \in \mathcal{F}_h^b, \end{cases} \qquad \sigma_p|_F = \gamma_p \min_{K^+,K^-} \left\{ \frac{h_K}{m} \right\} \quad F \in \mathcal{F}_h^i,$$

where γ_v and γ_p are two universal positive constants.

Next, we introduce three bilinear forms that are instrumental for the construction of the DG method. More precisely, we consider $a_h : [H^1(\mathcal{T}_h)]^d \times [H^1(\mathcal{T}_h)]^d \to \mathbb{R}$, $b_h : H^{\frac{1}{2}+\varepsilon}(\Omega) \times [H^1(\mathcal{T}_h)]^d \to \mathbb{R}$, and $s_h : H^{\frac{1}{2}+\varepsilon}(\Omega) \times H^{\frac{1}{2}+\varepsilon}(\Omega) \to \mathbb{R}$, for all $\varepsilon > 0$, defined as

$$a_h(\boldsymbol{u}, \boldsymbol{v}) = \int_\Omega \mu \nabla_h \boldsymbol{u} : \nabla_h \boldsymbol{v} - \sum_{F \in \mathcal{F}_h} \int_F \mu \{\nabla_h \boldsymbol{u}\} : [\![\boldsymbol{v}]\!] \tag{4a}$$

$$- \sum_{F \in \mathcal{F}_h} \int_F \mu \, [\![\boldsymbol{u}]\!] : \{\nabla_h \boldsymbol{v}\} + \sum_{F \in \mathcal{F}_h} \int_F \sigma_v \, [\![\boldsymbol{u}]\!] : [\![\boldsymbol{v}]\!], \tag{4b}$$

$$b_h(p, \boldsymbol{v}) = - \int_\Omega p \nabla_h \cdot \boldsymbol{v} + \sum_{F \in \mathcal{F}_h} \int_F \{p \boldsymbol{I}\} : [\![\boldsymbol{v}]\!], \tag{4c}$$

$$s_h(p, q) = \sum_{F \in \mathcal{F}_h^i} \int_F \sigma_p \, [\![p]\!] \cdot [\![q]\!], \tag{4d}$$

where ∇_h is the piecewise broken gradient operator.

Given $\boldsymbol{f} \in [L^2(\Omega)]^d$, the semi-discrete PolyDG approximation of (2) reads as follows: for any $t \in (0, T]$, find $(\boldsymbol{u}_h, p_h) \in \mathbf{V}_h^\ell \times Q_h^m$ such that

$$(\rho \partial_t \boldsymbol{u}_h, \boldsymbol{v}_h)_\Omega + a_h(\boldsymbol{u}_h, \boldsymbol{v}_h) + b_h(p_h, \boldsymbol{v}_h) - b_h(q_h, \boldsymbol{u}_h) + s_h(p_h, q_h) = (\boldsymbol{f}, \boldsymbol{v}_h)_\Omega \tag{5}$$

for all $(\boldsymbol{v}_h, q_h) \in \mathbf{V}_h^\ell \times Q_h^m$.

3 Well-posedness of the stationary Stokes problem

In this section, we prove the well-posedness of problem (5) in the stationary case making use of the Banach-Nečas-Babuška theorem.

To this aim, we first introduce

$$\mathcal{B}_h((\boldsymbol{u},p),(\boldsymbol{v},q)) = a_h(\boldsymbol{u},\boldsymbol{v}) + b_h(p,\boldsymbol{v}) - b_h(q,\boldsymbol{u}) + s_h(p,q), \qquad F((\boldsymbol{v},q)) = (\boldsymbol{f},\boldsymbol{v})_\Omega, \tag{6}$$

and re-write the stationary discrete Stokes problem as follows: find $(\boldsymbol{u}_h, p_h) \in \mathbf{V}_h^\ell \times Q_h^m$ such that

$$\mathcal{B}_h((\boldsymbol{u}_h,p_h),(\boldsymbol{v}_h,q_h)) = F((\boldsymbol{v}_h,q_h)) \qquad \forall (\boldsymbol{v}_h,q_h) \in \mathbf{V}_h^\ell \times Q_h^m. \tag{7}$$

On the product space $\mathbf{V}_h^\ell \times Q_h^m$, we define the norm

$$\|(\boldsymbol{v}_h,q_h)\|_{\mathrm{E}}^2 = \|\boldsymbol{v}_h\|_{\mathbf{V}_h^\ell}^2 + \|q_h\|_{Q_h^m}^2 \qquad \forall (\boldsymbol{v}_h,q_h) \in \mathbf{V}_h^\ell \times Q_h^m, \tag{8}$$

where

$$\begin{aligned} \|\boldsymbol{v}_h\|_{\mathbf{V}_h^\ell}^2 &= \sum_{K\in\mathcal{T}_k} \|\mu^{1/2}\nabla_h \boldsymbol{v}_h\|_{L^2(K)}^2 + \|\sigma_v^{1/2}[\![\boldsymbol{v}_h]\!]\|_{L^2(\mathcal{F}_h)}^2 \qquad \forall \boldsymbol{v}_h \in \mathbf{V}_h^\ell, \\ \|q_h\|_{Q_h^m}^2 &= \|q_h\|_{L^2(\Omega)}^2 + |q_h|_{\mathsf{J}}^2, \qquad |q_h|_{\mathsf{J}}^2 = s_h(q_h,q_h) \qquad \forall q_h \in Q_h^m. \end{aligned} \tag{9}$$

Before presenting the theoretical analysis, we introduce some mesh assumptions and technical results that will be needed in the forthcoming analysis.

3.1 Mesh assumptions and preliminary results

Following [25, 21, 4], we introduce the notion of a family of *polytopic-regular* meshes $\mathcal{T}_h$. To this end, we write τ_{K_F} to denote a d-dimensional simplex contained in $K \in \mathcal{T}_h$, which shares a specific face $F \subset \partial K$, $F \in \mathcal{F}_h$.

Definition 3.1 *A family of polytopic meshes $\{\mathcal{T}_h\}_h$ is said to be* polytopic-regular *if, for any h and $K \in \mathcal{T}_h$, there exists a set of non-overlapping (not necessarily shape-regular) d-dimensional simplices $\{\tau_{K_F}\}_{F\subset\partial K}$ contained in K, such that, for all faces $F \subset \partial K$,*

$$h_K \lesssim \frac{|\tau_{K_F}|}{|F|}.$$

The hidden constant is independent of the discretization parameters, the number of faces of the element, and the face measure.

This definition is very general as it does not require any restriction on either the number of faces per element or their relative measure. In particular, it allows the size of a face $F \subset \partial K$ to be arbitrarily small compared to the diameter of the element h_K it belongs to, provided that the height of the corresponding simplex τ_{K_F} is comparable to h_K; cf. [24] for more details.

In order to state suitable approximation results, cf. Lemmata 3.2 and 3.3 below and [25], we introduce a *shape-regular covering* $\mathcal{T}_h^{\#} = \{T_K\}$ of $\mathcal{T}_h$ defined as a set of shape-regular d-dimensional simplices T_K, such that, for each $K \in \mathcal{T}_h$, there exists a $T_K \in \mathcal{T}_h^{\#}$ such that $K \subsetneq T_K$.

We introduce the following assumption on the mesh $\mathcal{T}_h$; cf. [25, 24].

Assumption 3.1 *Given $\{\mathcal{T}_h\}_h$, $h > 0$, we assume that the following properties are uniformly satisfied:*

- ***A.1*** *$\mathcal{T}_h$ is uniformly* polytopic-regular *in the sense of Definition 3.1;*
- ***A.2*** *we assume that there exists a* shape-regular covering $\mathcal{T}_h^{\#}$ *of $\mathcal{T}_h$ such that, for each pair $K \in \mathcal{T}_h$, $\mathcal{K} \in \mathcal{T}_h^{\#}$ with $K \subset \mathcal{K}$, the following properties are fulfilled:* i) $h_{\mathcal{K}} \lesssim h_K$ *and* ii) $\max_{K \in \mathcal{T}_h} \mathrm{card}\{K' \in \mathcal{T}_h : K' \cap \mathcal{K} \neq \emptyset, \mathcal{K} \in \mathcal{T}_h^{\#}, K \subset \mathcal{K}\} \lesssim 1$;
- ***A.3*** *for any pair of elements $K, K' \in \mathcal{T}_h$ sharing a face $F \in \mathcal{F}_h$, we have: $h_K \lesssim h_{K'}$ and $h_{K'} \lesssim h_K$, where the hidden constants are independent of the discretization parameters as well as the number of faces of the two elements.*

The local bounded variation hypothesis **A.3** has been introduced so as to avoid technicalities.

The following trace-inverse inequality is valid; see, e.g., [24, Lemma 11].

Lemma 3.1 (Polynomial trace inverse inequality) *Let Assumption **A.1** be valid. For each $K \in \mathcal{T}_h$, the following trace-inverse inequality is valid:*

$$\|v\|^2_{L^2(\partial K)} \lesssim \frac{r^2}{h_K} \|v\|^2_{L^2(K)} \quad \forall v \in \mathcal{P}^r(K), \quad r \geq 1,$$

where the hidden constant is independent of r, h_K, and the number of faces of the element.

Let $\mathcal{E} : H^s(\Omega) \to H^s(\mathbb{R}^d)$, $s \geq 0$, be the Stein extension operator for Sobolev spaces on Lipschitz domains introduced in [51, Chapter 3]. The operator $\mathcal{E}$ satisfies the following property: given a domain Ω with Lipschitz boundary, for all $q \in H^s(\Omega)$,

$$\mathcal{E}(q)|_\Omega = q, \qquad \|\mathcal{E}q\|_{H^s(\mathbb{R}^d)} \lesssim \|q\|_{H^s(\Omega)}. \tag{10}$$

For vector-valued functions, the Stein extension operator is defined component-wise. We recall the following approximation result; see, e.g., [25, 21, 24] for a detailed proof, which generalizes the standard arguments for standard geometries [8, 9].

Lemma 3.2 (Best polynomial approximation in Sobolev norms) *Let Assumption **A.2** be valid. Given the Stein extension operator $\mathcal{E}$ in (10), let $v \in L^2(\Omega)$*

be such that $(\mathcal{E}v)\,|_{\mathcal{K}} \in H^r(\mathcal{K})$*, for some* $r \geq 0$*. Then, there exists a sequence of polynomial approximations* $\Pi_K^\ell v \in \mathcal{P}_\ell(K)$ *of* v*,* $K \in \mathcal{T}_h$ *and* $\ell \in \mathbb{N}$ *of* v *satisfying*

$$\|v - \Pi_K^\ell v\|_{H^q(K)} \lesssim \frac{h_K^{\min\{\ell+1,r\}-q}}{\ell^{r-q}} \|\mathcal{E}v\|_{H^r(\mathcal{K})}, \qquad 0 \leq q \leq r,$$

where $\mathcal{K} \in \mathcal{T}_h^\#$ *is the* d*-simplex of* $\mathcal{T}_h^\#$ *such that* $K \subset \mathcal{K}$*. Moreover, if* $v \in H^1(\Omega)$ *is such that* $(\mathcal{E}v)\,|_{\mathcal{K}} \in H^r(\mathcal{K})$*, for some* $r \geq 1$*, then we have*

$$\|v - \Pi_K^\ell v\|_{L^2(\partial K)} \lesssim \frac{h_K^{\min\{\ell+1,r\}-1/2}}{\ell^{r-1/2}} \|\mathcal{E}v\|_{H^r(\mathcal{K})}, \qquad r \geq 1.$$

The hidden constants are independent of the discretization parameters as well as the number of faces of the element.

Based on employing the above result, we define the global polynomial approximation operator $\Pi^\ell v$ as

$$(\Pi^\ell v)|_K = \Pi_K^\ell (v|_K) \qquad \forall K \in \mathcal{T}_h.$$

For vector-valued functions, the operators Π_K^ℓ and Π^ℓ are defined component-wise and are still denoted by Π_K^ℓ and Π^ℓ, respectively.

We have the following approximation bound in the energy norm (9).

Lemma 3.3 (Best polynomial approximation in the DG norm) *Let Assumption 3.1 be valid. Let* $\boldsymbol{v} \in [L^2(\Omega)]^d$ *be such that, for some* $r \geq 1$*,* $(\mathcal{E}v)\,|_{\mathcal{K}} \in [H^r(\mathcal{K})]^d$ *for all* $\mathcal{K} \in \mathcal{T}_h^\#$*,* $r \geq 1$*. Then, we have*

$$\|\boldsymbol{v} - \Pi^\ell \boldsymbol{v}\|_{\mathbf{V}_h^\ell}^2 \lesssim \sum_{K \in \mathcal{T}_h} \frac{h_K^{2(\min\{\ell+1,r\}-1)}}{\ell^{2(r-1)-1}} \|\mathcal{E}\boldsymbol{v}\|_{H^r(\mathcal{K})}^2.$$

The hidden constants are independent of the discretization parameters as well as the number of faces of each element.

The suboptimality in terms of the polynomial degree in the estimates of Lemma 3.3 is due to the presence of the stabilization term and the suboptimality of the polynomial trace inverse estimate of Lemma 3.1.

Finally, we recall the following continuity and coercivity bounds for the bilinear form $a_h(\cdot,\cdot)$. The proof is based upon employing the trace-inverse estimate in Lemma 3.1 and standard arguments for DG methods; see, e.g., [24].

Lemma 3.4 (Coercivity and continuity of $a_h(\cdot,\cdot)$**)** *Let Assumption 3.1 be valid. Then, we have*

$$a_h(\boldsymbol{v}_h, \boldsymbol{v}_h) \gtrsim \|\boldsymbol{v}_h\|_{\mathbf{V}_h^\ell}^2 \qquad \forall \boldsymbol{v}_h \in \mathbf{V}_h^\ell,$$

and

$$|a_h(\boldsymbol{u}_h, \boldsymbol{v}_h)| \lesssim \|\boldsymbol{u}_h\|_{\mathbf{V}_h^\ell} \|\boldsymbol{v}_h\|_{\mathbf{V}_h^\ell} \qquad \forall \boldsymbol{u}_h, \boldsymbol{v}_h \in \mathbf{V}_h^\ell.$$

The coercivity bounds are achieved provided that the penalty parameter γ_v in Definition 2.1 of the penalty function σ_v is chosen sufficiently large. The hidden constants are independent of the discretization parameters, the number of faces per element, and the relative size of a face compared to the diameter of the element it belongs to.

3.2 Generalized *inf-sup* condition

In this section, we prove a generalized *inf-sup* condition for the discrete bilinear form $b_h(\cdot,\cdot)$ defined in (4c). First, we need some preliminary results.

Lemma 3.5 (Boundedness of Π^ℓ in the energy norm (9)) *Let Assumption 3.1 be valid. Then, we have*

$$\|\Pi^\ell \boldsymbol{v}\|_{\mathbf{V}_h^\ell} \lesssim \ell^{1/2} \|\boldsymbol{v}\|_{H^1(\Omega)} \quad \forall \boldsymbol{v} \in \boldsymbol{V}.$$

The hidden constants are independent of the discretization parameters as well as the number of faces of the element.

Proof. Given $\boldsymbol{v} \in \boldsymbol{V}$, using the definition (9) of the energy norm and the fact that $[\![\boldsymbol{v}]\!] = \mathbf{0}$ on $F \in \mathcal{F}_h$, we immediately have

$$\|\Pi^\ell \boldsymbol{v}\|_{\mathbf{V}_h^\ell}^2 \le \|\Pi^\ell \boldsymbol{v} - \boldsymbol{v}\|_{\mathbf{V}_h^\ell}^2 + \|\boldsymbol{v}\|_{\mathbf{V}_h^\ell}^2 \lesssim \|\Pi^\ell \boldsymbol{v} - \boldsymbol{v}\|_{\mathbf{V}_h^\ell}^2 + \|\boldsymbol{v}\|_{H^1(\Omega)}^2.$$

Using Lemma 3.3 with $r = 1$, Assumption **A.2**, and the continuity of the Stein operator $\mathcal{E}$ in (10), we get

$$\|\Pi^\ell \boldsymbol{v}\|_{\mathbf{V}_h^\ell}^2 \lesssim \sum_{K \in \mathcal{T}_h} \ell \|\mathcal{E}\boldsymbol{v}\|_{H^1(\mathcal{K})}^2 + \|\boldsymbol{v}\|_{H^1(\Omega)}^2 \lesssim (1+\ell)\|\boldsymbol{v}\|_{H^1(\Omega)}^2.$$

□

Next, we introduce the L^2 projector onto the space $\mathbf{V}_h^\ell$:

$$\Pi_0^\ell : [L^2(\Omega)]^d \longrightarrow \mathbf{V}_h^\ell, \qquad \left(\boldsymbol{w}_h, \boldsymbol{v} - \Pi_0^\ell \boldsymbol{v}\right)_{L^2(\Omega)} = 0 \quad \forall \boldsymbol{w}_h \in \mathbf{V}_h^\ell,$$

and state the following result, which is based on a further assumption and a technical result; see Assumption 3.2 and Lemma 3.6 below, respectively.

Assumption 3.2 *Given $\{\mathcal{T}_h\}_h$, $h > 0$, each element $K \in \mathcal{T}_h$ admits a decomposition into shape-regular simplices having size comparable to that of K.*

The following inverse estimate on shape-regular polygons can be found, e.g., in [24, Lemma 14]. It generalizes a similar result for standard geometries; see, e.g., [50, Theorem 4.76].

Lemma 3.6 ($H^1 - L^2$ polynomial inverse estimate) *Let Assumption 3.2 be valid. For each $K \in \mathcal{T}_h$, the following polynomial inverse inequality is valid:*

$$\|\nabla v\|^2_{L^2(K)} \lesssim \frac{\ell^4}{h_K^2}\|v\|^2_{L^2(K)} \quad \forall v \in \mathcal{P}^\ell(K), \quad \ell \geq 1.$$

The hidden constant is independent of ℓ, h_K, and the number of faces of the element.

Based on employing the above result, we prove the following bound.

Lemma 3.7 (Stability properties of orthogonal projections) *Let Assumptions 3.1 and 3.2 be valid. Then, we have*

$$\|\Pi_0^\ell(\boldsymbol{v} - \Pi^\ell \boldsymbol{v})\|_{\mathbf{V}_h^\ell} \lesssim \ell \|\boldsymbol{v}\|_{\boldsymbol{V}} \quad \forall \boldsymbol{v} \in \boldsymbol{V}.$$

The hidden constant is independent of the discretization parameters as well as the number of faces of the element.

Proof. From the definition of the energy norm (9), the inverse estimate in Lemma 3.6, the stability of the projector Π_0^ℓ in the L^2 norm, the polynomial approximation properties of Lemma 3.2, and the continuity of the Stein operator $\mathcal{E}$ in (10), we have

$$\begin{aligned}\sum_{K\in\mathcal{T}_h} |\Pi_0^\ell(\boldsymbol{v} - \Pi^\ell \boldsymbol{v})|^2_{H^1(K)} &\lesssim \sum_{K\in\mathcal{T}_h} \frac{\ell^4}{h_K^2}\|\Pi_0^\ell(\boldsymbol{v} - \Pi^\ell \boldsymbol{v})\|^2_{L^2(K)} \\ &\leq \sum_{K\in\mathcal{T}_h} \frac{\ell^4}{h_K^2}\|\boldsymbol{v} - \Pi^\ell \boldsymbol{v}\|^2_{L^2(K)} \lesssim \ell^2 \|\boldsymbol{v}\|^2_{\boldsymbol{V}}.\end{aligned}$$

Next, using the definition of σ_v in Definition 2.1, the discrete trace-inverse inequality in Lemma 3.1, the continuity of the L^2-projector, the approximation results in Lemma 3.2, and the continuity of the Stein operator $\mathcal{E}$ in (10), and Assumption **A.2**, we have

$$\begin{aligned}\|\sigma_v^{1/2}\, [\![\Pi_0^\ell(\boldsymbol{v} - \Pi^\ell \boldsymbol{v})]\!]\|^2_{L^2(\mathcal{F}_h)} &\lesssim \sum_{K\in\mathcal{T}_h} \frac{\ell^2}{h_K}\|\Pi_0^\ell(\boldsymbol{v} - \Pi^\ell \boldsymbol{v})\|^2_{L^2(\partial K)} \\ &\lesssim \sum_{K\in\mathcal{T}_h} \frac{\ell^4}{h_K^2}\|\Pi_0^\ell(\boldsymbol{v} - \Pi^\ell \boldsymbol{v})\|^2_{L^2(K)} \lesssim \sum_{K\in\mathcal{T}_h} \frac{\ell^4}{h_K^2}\|\boldsymbol{v} - \Pi^\ell \boldsymbol{v}\|^2_{L^2(K)} \\ &\lesssim \sum_{K\in\mathcal{T}_h} \frac{\ell^4}{h_K^2}\frac{h_K^2}{\ell^2}\|\mathcal{E}\boldsymbol{v}\|^2_{H^1(\mathcal{K})} \lesssim \ell^2 \|\boldsymbol{v}\|^2_{\boldsymbol{V}}.\end{aligned}$$

The assertion follows summing up the two bounds. □

Remark 3.1 *Assumption 3.2 is required in the proof of the polynomial inverse estimate of Lemma 3.6. On the other hand, the suboptimality in terms of the polynomial degree in the stability properties detailed in Lemma 3.7 is now due to both the inverse estimates of Lemmata 3.1 and 3.6. This propagates further in the proof of the discrete inf-sup condition, see Proposition 3.1 below, and consequently to the abstract and convergence analysis detailed in Section 5 below.*

Remark 3.2 *Following the recent approach of [22], it is possible to prove the inverse estimates in Lemmata 3.1 and 3.6 using assumptions milder than Assumptions 3.1 and 3.2. Notably, the theory therein presented covers very general geometries, including $\mathcal{C}^1$-curved faces and possibly the presence of arbitrary number of faces.*

Next, we show that a generalized *inf-sup* condition is valid, provided that the polynomial degrees ℓ and m of the discrete velocity and pressure spaces satisfy $m - \ell \leq 1$. This condition guarantees in fact that $\nabla Q_h^m \subseteq \mathbf{V}_h^\ell$.

Proposition 3.1 (Generalized *inf-sup* condition for $b_h(\cdot,\cdot)$)
Let Assumptions 3.1 and 3.2 be valid and assume that the polynomial degrees ℓ and m of the discrete velocity and pressure spaces satisfy $m - \ell \leq 1$. Then, the following bound is valid:

$$\sup_{\mathbf{0}\neq \boldsymbol{v}_h \in \mathbf{V}_h^\ell} \frac{b_h(q_h, \boldsymbol{v}_h)}{\|\boldsymbol{v}_h\|_{\mathbf{V}_h^\ell}} + |q_h|_{\mathsf{J}} \geq \beta_h \|q_h\|_{L^2(\Omega)} \quad \forall q_h \in Q_h^m,$$

where the discrete inf-sup constant behaves as

$$\beta_h = O\left(\frac{\beta}{\max\left\{\ell^{1/2}(1+\ell^{1/2}), m^{1/2}+1\right\}}\right). \tag{11}$$

Proof. Upon employing element-wise integration by parts, the bilinear form $b_h(\cdot,\cdot)$ defined as

$$b_h(q_h, \boldsymbol{v}_h) = -\int_\Omega q_h \nabla_h \cdot \boldsymbol{v}_h + \sum_{F\in\mathcal{F}_h} \int_F \{q_h \boldsymbol{I}\} : [\![\boldsymbol{v}_h]\!] \qquad \forall q_h \in Q_h^m, \boldsymbol{v}_h \in \mathbf{V}_h^\ell,$$

can be equivalently rewritten as

$$b_h(q_h, \boldsymbol{v}_h) = \int_\Omega \nabla_h q_h \cdot \boldsymbol{v}_h - \sum_{F\in\mathcal{F}_h^I} \int_F [\![q_h]\!] \cdot \{\boldsymbol{v}_h\} \qquad \forall q_h \in Q_h^m, \boldsymbol{v}_h \in \mathbf{V}_h^\ell.$$

Recall the continuous *inf-sup* condition (3): there exists $\beta > 0$ such that, to each $q_h \in Q_h^m \subset L_0^2(\Omega)$, we associate $\boldsymbol{v}_{q_h} \in \boldsymbol{V}$ with

$$\nabla \cdot \boldsymbol{v}_{q_h} = q_h, \qquad \beta \|\boldsymbol{v}_{q_h}\|_{\boldsymbol{V}} \leq \|q_h\|_{L^2(\Omega)}. \tag{12}$$

Then, applying element-wise integration by parts, using that $[\![\boldsymbol{v}_{q_h}]\!] = \mathbf{0}$ for any $F \in \mathcal{F}_h$, and

observing that $\nabla_h q_h \in \mathbf{V}_h^\ell$ if $\ell \geq m-1$, we obtain

$$
\begin{aligned}
\|q_h\|_{L^2(\Omega)}^2 &= \int_\Omega q_h \nabla\cdot \boldsymbol{v}_{q_h} = -\int_\Omega \nabla_h q_h \cdot \boldsymbol{v}_{q_h} + \sum_{F\in\mathcal{F}_h}\int_F [\![q_h]\!] : \{\boldsymbol{v}_{q_h}\} \\
&= -\int_\Omega \nabla_h q_h \cdot \Pi^\ell \boldsymbol{v}_{q_h} + \int_\Omega \nabla_h q_h \cdot (\Pi^\ell \boldsymbol{v}_{q_h} - \boldsymbol{v}_{q_h}) + \sum_{F\in\mathcal{F}_h}\int_F [\![q_h]\!] \cdot \{\boldsymbol{v}_{q_h}\} \\
&= \int_\Omega q_h \nabla\cdot \Pi^\ell \boldsymbol{v}_{q_h} + \int_\Omega \nabla_h q_h \cdot (\Pi^\ell \boldsymbol{v}_{q_h} - \boldsymbol{v}_{q_h}) \\
&\quad - \sum_{F\in\mathcal{F}_h}\int_F \{q_h \boldsymbol{I}\} : [\![\Pi^\ell \boldsymbol{v}_{q_h}]\!] + \sum_{F\in\mathcal{F}_h}\int_F [\![q_h]\!] \cdot \{\boldsymbol{v}_{q_h} - \Pi^\ell \boldsymbol{v}_{q_h}\} \\
&= \underbrace{-b_h\left(q_h, \Pi^\ell \boldsymbol{v}_{q_h}\right)}_{\text{(A)}} + \underbrace{\int_\Omega \nabla_h q_h \cdot (\Pi^\ell \boldsymbol{v}_{q_h} - \boldsymbol{v}_{q_h})}_{\text{(B)}} + \underbrace{\sum_{F\in\mathcal{F}_h}\int_F [\![q_h]\!] \cdot \{\boldsymbol{v}_{q_h} - \Pi^\ell \boldsymbol{v}_{q_h}\}}_{\text{(C)}}.
\end{aligned}
\tag{13}
$$

We bound the three terms on the right-hand side of (13) separately. As for the term (A), thanks to the boundedness of Π^ℓ in the energy norm, see Lemma 3.5, and the continuous *inf-sup* condition (12), we get

$$
\begin{aligned}
\text{(A)} = -b_h\left(q_h, \Pi^\ell \boldsymbol{v}_{q_h}\right) &\leq \frac{\left|b_h\left(q_h, \Pi^\ell \boldsymbol{v}_{q_h}\right)\right|}{\|\Pi^\ell \boldsymbol{v}_{q_h}\|_{\mathbf{V}_h^\ell}} \|\Pi^\ell \boldsymbol{v}_{q_h}\|_{\mathbf{V}_h^\ell} \\
&\lesssim \ell^{1/2} \frac{\left|b_h\left(q_h, \Pi^\ell \boldsymbol{v}_{q_h}\right)\right|}{\|\Pi^\ell \boldsymbol{v}_{q_h}\|_{\mathbf{V}_h^\ell}} \|\boldsymbol{v}_{q_h}\|_{H^1(\Omega)} \leq \frac{\ell^{1/2}}{\beta} \frac{\left|b_h\left(q_h, \Pi^\ell \boldsymbol{v}_{q_h}\right)\right|}{\|\Pi^\ell \boldsymbol{v}_{q_h}\|_{\mathbf{V}_h^\ell}} \|q_h\|_{L^2(\Omega)} \\
&\leq \frac{\ell^{1/2}}{\beta} \|q_h\|_{L^2(\Omega)} \sup_{\boldsymbol{v}_h \in \mathbf{V}_h^\ell \setminus \{\mathbf{0}\}} \frac{b_h\left(q_h, \boldsymbol{v}_h\right)}{\|\boldsymbol{v}_h\|_{\mathbf{V}_h^\ell}}.
\end{aligned}
\tag{14}
$$

As for the term (C), using the Cauchy-Schwarz inequality, the definition of the penalty function σ_p in Definition 2.1, Assumption **A.3**, the second bound in Lemma 3.2 with $r=1$, and $m-\ell \leq 1$, we obtain

$$
\begin{aligned}
\text{(C)} &\lesssim |q_h|_{\text{J}} \left(\sum_{K\in\mathcal{T}_h} \frac{m}{h_K} \|\boldsymbol{v}_{q_h} - \Pi^\ell \boldsymbol{v}_{q_h}\|_{L^2(\partial K)}^2\right)^{1/2} \\
&\lesssim |q_h|_{\text{J}} \left(\sum_{K\in\mathcal{T}_h} \frac{m}{h_K} \frac{h_K}{\ell} \|\mathcal{E}\boldsymbol{v}_{q_h}\|_{H^1(\mathcal{K})}^2\right)^{1/2} \lesssim |q_h|_{\text{J}} \left(\sum_{K\in\mathcal{T}_h} \|\mathcal{E}\boldsymbol{v}_{q_h}\|_{H^1(\mathcal{K})}^2\right)^{1/2}.
\end{aligned}
$$

Finally, using the continuity of the Stein extension operator $\mathcal{E}$ in (10), Assumption **A.3**, and the continuous *inf-sup* condition (12), we get

$$
\text{(C)} \lesssim |q_h|_{\text{J}} \|\boldsymbol{v}_{q_h}\|_{H^1(\Omega)} \leq \frac{1}{\beta} |q_h|_{\text{J}} \|q_h\|_{L^2(\Omega)}. \tag{15}
$$

As for the term (B), using the definition of L^2 projector, the fact that $\nabla_h q_h \in \mathbf{V}_h^\ell$ $(m-\ell \leq 1)$,

and an integration by parts, we write

$$
\begin{aligned}
\textcircled{B} &= \int_\Omega \nabla_h q_h \cdot (\Pi^\ell \boldsymbol{v}_{q_h} - \Pi_0^\ell \boldsymbol{v}_{q_h} + \Pi_0^\ell \boldsymbol{v}_{q_h} - \boldsymbol{v}_{q_h}) = \int_\Omega \nabla_h q_h \cdot (\Pi^\ell \boldsymbol{v}_{q_h} - \Pi_0^\ell \boldsymbol{v}_{q_h}) \\
&= \int_\Omega \nabla_h q_h \cdot (\Pi_0^\ell \Pi^\ell \boldsymbol{v}_{q_h} - \Pi_0^\ell \boldsymbol{v}_{q_h}) = \int_\Omega \nabla_h q_h \cdot \Pi_0^\ell (\Pi^\ell \boldsymbol{v}_{q_h} - \boldsymbol{v}_{q_h}) \\
&= \underbrace{b_h(q_h, \Pi_0^\ell(\Pi^\ell \boldsymbol{v}_{q_h} - \boldsymbol{v}_{q_h}))}_{\textcircled{I}} + \underbrace{\sum_{F \in \mathcal{F}_h^i} \int_F [\![q_h]\!] \cdot \{\Pi_0^\ell(\Pi^\ell \boldsymbol{v}_{q_h} - \boldsymbol{v}_{q_h}))\}}_{\textcircled{II}}.
\end{aligned}
\tag{16}
$$

We bound the two terms on the right-hand side separately. As for the term Ⓘ, we proceed as above, namely we use the continuity of the Stein extension operator $\mathcal{E}$ in (10), Assumption **A.2**, and the continuous *inf-sup* condition (12):

$$
\begin{aligned}
\textcircled{I} &\leq \frac{\left| b_h\left(q_h, \Pi_0^\ell(\Pi^\ell \boldsymbol{v}_{q_h} - \boldsymbol{v}_{q_h})\right)\right|}{\|\Pi_0^\ell(\Pi^\ell \boldsymbol{v}_{q_h} - \boldsymbol{v}_{q_h})\|_{\mathbf{V}_h^\ell}} \|\Pi_0^\ell(\Pi^\ell \boldsymbol{v}_{q_h} - \boldsymbol{v}_{q_h})\|_{\mathbf{V}_h^\ell} \\
&\leq \left(\sup_{\boldsymbol{v}_h \in \mathbf{V}_h^\ell \setminus \{\mathbf{0}\}} \frac{b_h\left(q_h, \boldsymbol{v}_h\right)}{\|\boldsymbol{v}_h\|_{\mathbf{V}_h^\ell}} \right) \|\Pi_0^\ell(\Pi^\ell \boldsymbol{v}_{q_h} - \boldsymbol{v}_{q_h})\|_{\mathbf{V}_h^\ell} \\
&\lesssim \ell \left(\sup_{\boldsymbol{v}_h \in \mathbf{V}_h^\ell \setminus \{\mathbf{0}\}} \frac{b_h\left(q_h, \boldsymbol{v}_h\right)}{\|\boldsymbol{v}_h\|_{\mathbf{V}_h^\ell}} \right) \|\boldsymbol{v}_{q_h}\|_{\boldsymbol{V}} \leq \frac{\ell}{\beta} \left(\sup_{\boldsymbol{v}_h \in \mathbf{V}_h^\ell \setminus \{\mathbf{0}\}} \frac{b_h\left(q_h, \boldsymbol{v}_h\right)}{\|\boldsymbol{v}_h\|_{\mathbf{V}_h^\ell}} \right) \|q_h\|_{L^2(\Omega)}.
\end{aligned}
\tag{17}
$$

As for the term Ⓘⓘ, we make use of the trace-inverse inequality of Lemma 3.1, the stability in L^2 of the projector Π_0^ℓ, the interpolation bounds of Lemma 3.2, the continuity of the Stein extension operator $\mathcal{E}$ in (10) together with Assumption **A.2**, and the continuous *inf-sup* condition (12) to obtain

$$
\begin{aligned}
\textcircled{II} &\lesssim |q_h|_{\mathsf{J}} \left(\sum_{K \in \mathcal{T}_h} \frac{m}{h_K} \|\Pi_0^\ell(\Pi^\ell \boldsymbol{v}_{q_h} - \boldsymbol{v}_{q_h})\|_{L^2(\partial K)}^2 \right)^{1/2} \\
&\lesssim |q_h|_{\mathsf{J}} \left(\sum_{K \in \mathcal{T}_h} \frac{m}{h_K} \frac{\ell^2}{h_K} \|\Pi_0^\ell(\Pi^\ell \boldsymbol{v}_{q_h} - \boldsymbol{v}_{q_h})\|_{L^2(K)}^2 \right)^{1/2} \\
&\lesssim |q_h|_{\mathsf{J}} \left(\sum_{K \in \mathcal{T}_h} \frac{m}{h_K} \frac{\ell^2}{h_K} \frac{h_K^2}{\ell^2} \|\mathcal{E} \boldsymbol{v}_{q_h}\|_{H^1(\mathcal{K})}^2 \right)^{1/2} \\
&\lesssim m^{1/2} |q_h|_{\mathsf{J}} \|\boldsymbol{v}_{q_h}\|_{H^1(\Omega)} \leq \frac{m^{1/2}}{\beta} |q_h|_{\mathsf{J}} \|q_h\|_{L^2(\Omega)}.
\end{aligned}
\tag{18}
$$

Inserting the two bounds (17) and (18) into (16), we obtain

$$
\textcircled{B} \lesssim \frac{\ell}{\beta} \left(\sup_{\boldsymbol{v}_h \in \mathbf{V}_h^\ell \setminus \{\mathbf{0}\}} \frac{b_h\left(q_h, \boldsymbol{v}_h\right)}{\|\boldsymbol{v}_h\|_{\mathbf{V}_h^\ell}} \right) \|q_h\|_{L^2(\Omega)} + \frac{m^{1/2}}{\beta} |q_h|_{\mathsf{J}} \|q_h\|_{L^2(\Omega)}. \tag{19}
$$

Collecting (14), (15), and (19) into (13), we arrive at

$$\begin{aligned}\|q_h\|_{L^2(\Omega)} &\lesssim \left(\frac{\ell^{1/2}+\ell}{\beta}\right) \sup_{\boldsymbol{v}_h \in \mathbf{V}_h^\ell \setminus \{\mathbf{0}\}} \frac{b_h\left(q_h, \boldsymbol{v}_h\right)}{\|\boldsymbol{v}_h\|_{\mathbf{V}_h^\ell}} + \left(\frac{m^{1/2}+1}{\beta}\right) |q_h|_{\mathrm{J}} \\ &\lesssim \frac{1}{\beta} \max\left\{\ell^{1/2}(1+\ell^{1/2}), m^{1/2}+1\right\} \left(\sup_{\boldsymbol{v}_h \in \mathbf{V}_h^\ell \setminus \{\mathbf{0}\}} \frac{b_h\left(q_h, \boldsymbol{v}_h\right)}{\|\boldsymbol{v}_h\|_{\mathbf{V}_h^\ell}} + |q_h|_{\mathrm{J}} \right).\end{aligned}$$

The assertion follows with the discrete generalized *inf-sup* constant having the behaviour in (11). □

Remark 3.3 *The constant of the generalized inf-sup condition stated in Proposition 3.1 is uniform with respect to the mesh size but depends on the polynomial approximation degrees ℓ and m; see (11). This implies that $\beta_h \searrow 0$ as $\ell, m \nearrow +\infty$.*

In Section 4, we will present some computations to assess numerically the sharpness of the inf-sup constant β_h, for different mesh configurations and polynomial orders. We will find out that Assumption 3.2 does not seem necessary in the proof of Proposition 3.1. The analysis with milder assumptions is under investigation.

3.3 Well-posedness of the discret Stokes problem via the Banach-Nečas-Babuška theorem.

To prove that the discrete problem (7) is well-posed, we first recall the following abstract result; see, e.g, [33].

Theorem 3.1 (Banach-Nečas-Babuška) *Let $\mathcal{W}$ be a Banach space and $\mathcal{V}$ a reflexive Banach space. Let $B \in \mathcal{L}(\mathcal{W} \times \mathcal{V}; \mathbb{R})$ and $f \in \mathcal{V}'$, where $\mathcal{V}'$ is the dual space of V. Then, the problem*

$$\text{find } u \in \mathcal{W} \quad \text{such that} \quad B(u,v) = f(v) \quad \forall v \in \mathcal{V}$$

is well-posed if and only if

$$\exists \alpha > 0 \quad \inf_{w \in \mathcal{W}} \sup_{v \in \mathcal{V}} \frac{B(w,v)}{\|w\|_{\mathcal{W}} \|v\|_{\mathcal{V}}} \geq \alpha; \qquad \text{[BNB(i)]}$$

$$\forall v \in \mathcal{V} \quad (\forall w \in \mathcal{W} \quad B(w,v) = 0) \quad \Rightarrow \quad (v = 0). \qquad \text{[BNB(ii)]}$$

In the following, we set $B_h : \mathbf{V}_h^\ell \times Q_h^m \longrightarrow \mathbf{V}_h^\ell \times Q_h^m$ defined as

$$(B_h(\boldsymbol{v}_h, q_h), (\boldsymbol{w}_h, z_h))_{L^2(\Omega)} = \mathcal{B}_h((\boldsymbol{v}_h, q_h); (\boldsymbol{w}_h, z_h))$$

$\forall (\boldsymbol{v}_h, q_h), (\boldsymbol{w}_h, z_h) \in \mathbf{V}_h^\ell \times Q_h^m$. Under the hypotheses of Proposition 3.1, we show that [BNB(i)] and [BNB(ii)] are valid for the choice $B = B_h$, $\mathcal{W} = \mathcal{V} = \mathbf{V}_h^\ell \times Q_h^m$ endowed with the energy norm $\|(\cdot,\cdot)\|_{\mathrm{E}}$. This implies that problem (7) is well-posed.

To this aim, we notice that

$$\begin{aligned}\mathcal{B}_h((\boldsymbol{u}_h,p_h);(\boldsymbol{u}_h,p_h)) &= a_h(\boldsymbol{u}_h,\boldsymbol{u}_h)+b_h(p_h,\boldsymbol{u}_h)-b_h(p_h,\boldsymbol{u}_h)+s_h(p_h,p_h)\\ &\gtrsim \|\boldsymbol{u}_h\|^2_{\mathbf{V}_h^\ell}+|p_h|^2_{\mathrm{J}} \qquad \forall\,(\boldsymbol{u}_h,p_h)\in\mathbf{V}_h^\ell\times Q_h^m,\end{aligned} \tag{20}$$

provided that Assumption 3.1 is valid and the stabilization constant γ_v appearing in Definition 2.1 is chosen sufficiently large.

Proof. [Proof of [BNB(i)]] Given $(\boldsymbol{u}_h,p_h)\in\mathbf{V}_h^\ell\times Q_h^m$, we have

$$\mathcal{B}_h((\boldsymbol{u}_h,p_h);(\boldsymbol{u}_h,p_h))\le\mathbb{M}\|(\boldsymbol{u}_h,p_h)\|_{\mathrm{E}}, \tag{21}$$

where $\|\cdot\|_{\mathrm{E}}$ is defined as in (8) and

$$\mathbb{M}=\sup_{\substack{(\boldsymbol{v}_h,q_h)\in\mathbf{V}_h^\ell\times Q_h^m\\(\boldsymbol{v}_h,q_h)\neq(\mathbf{0},0)}}\frac{\mathcal{B}_h((\boldsymbol{u}_h,p_h);(\boldsymbol{v}_h,q_h))}{\|(\boldsymbol{v}_h,q_h)\|_{\mathrm{E}}}.$$

Using (20) and (21), we get

$$\|\boldsymbol{u}_h\|^2_{\mathbf{V}_h^\ell}+|p_h|^2_{\mathrm{J}}\lesssim\mathcal{B}_h((\boldsymbol{u}_h,p_h);(\boldsymbol{u}_h,p_h))\le\mathbb{M}\|(\boldsymbol{u}_h,p_h)\|_{\mathrm{E}}. \tag{22}$$

Thanks to Proposition 3.1 and to the fact that

$$b_h(p_h,\boldsymbol{v}_h)=\mathcal{B}_h((\boldsymbol{u}_h,p_h),(\boldsymbol{v}_h,0))-a_h(\boldsymbol{u}_h,\boldsymbol{v}_h)\quad\forall\boldsymbol{v}_h\in\mathbf{V}_h^\ell,$$

we have

$$\begin{aligned}\beta_h\|p_h\|_{L^2(\Omega)}&\le\sup_{\mathbf{0}\neq\boldsymbol{v}_h\in\mathbf{V}_h^\ell}\frac{b_h(p_h,\boldsymbol{v}_h)}{\|\boldsymbol{v}_h\|_{\mathbf{V}_h^\ell}}+|p_h|_{\mathrm{J}}\\&=\sup_{\mathbf{0}\neq\boldsymbol{v}_h\in\mathbf{V}_h^\ell}\frac{\mathcal{B}_h((\boldsymbol{u}_h,p_h),(\boldsymbol{v}_h,0))-a_h(\boldsymbol{u}_h,\boldsymbol{v}_h)}{\|\boldsymbol{v}_h\|_{\mathbf{V}_h^\ell}}+|p_h|_{\mathrm{J}}\\&\le\sup_{\mathbf{0}\neq\boldsymbol{v}_h\in\mathbf{V}_h^\ell}\frac{|\mathcal{B}_h((\boldsymbol{u}_h,p_h),(\boldsymbol{v}_h,0))|}{\|(\boldsymbol{v}_h,0)\|_{\mathrm{E}}}+\sup_{\mathbf{0}\neq\boldsymbol{v}_h\in\mathbf{V}_h^\ell}\frac{|a_h(\boldsymbol{u}_h,\boldsymbol{v}_h)|}{\|\boldsymbol{v}_h\|_{\mathbf{V}_h^\ell}}+|p_h|_{\mathrm{J}}\\&\lesssim\sup_{\mathbf{0}\neq\boldsymbol{v}_h\in\mathbf{V}_h^\ell}\frac{|\mathcal{B}_h((\boldsymbol{u}_h,p_h),(\boldsymbol{v}_h,0))|}{\|(\boldsymbol{v}_h,0)\|_{\mathrm{E}}}+\|\boldsymbol{u}_h\|_{\mathbf{V}_h^\ell}+|p_h|_{\mathrm{J}}\\&=\mathbb{M}+\|\boldsymbol{u}_h\|_{\mathbf{V}_h^\ell}+|p_h|_{\mathrm{J}}.\end{aligned}$$

Using (22), we deduce

$$\beta_h^2\|p_h\|^2_{L^2(\Omega)}\lesssim\mathbb{M}^2+\|\boldsymbol{u}_h\|^2_{\mathbf{V}_h^\ell}+|p_h|^2_{\mathrm{J}}\le\mathbb{M}^2+\mathbb{M}\|(\boldsymbol{u}_h,p_h)\|_{\mathrm{E}}.$$

From the definition of $\|(\cdot,\cdot)\|_{\mathrm{E}}$, using again (22), the above bound, and the Young's inequality with a positive parameter γ, we have

$$\begin{aligned}\beta_h^2\|(\boldsymbol{u}_h,p_h)\|^2_{\mathrm{E}}&=\beta_h^2(\|\boldsymbol{u}_h\|^2_{\mathbf{V}_h^\ell}+\|p_h\|^2_{L^2(\Omega)}+|p_h|^2_{\mathrm{J}})\\&\lesssim\beta_h^2\mathbb{M}\|(\boldsymbol{u}_h,p_h)\|_{\mathrm{E}}+\beta_h^2\|p_h\|^2_{L^2(\Omega)}\lesssim\beta_h^2\mathbb{M}\|(\boldsymbol{u}_h,p_h)\|_{\mathrm{E}}+\mathbb{M}^2+\mathbb{M}\|(\boldsymbol{u}_h,p_h)\|_{\mathrm{E}}\\&=(1+\beta_h^2)\mathbb{M}\|(\boldsymbol{u}_h,p_h)\|_{\mathrm{E}}+\mathbb{M}^2\le\gamma\|(\boldsymbol{u}_h,p_h)\|^2_{\mathrm{E}}+\left(1+\frac{(1+\beta_h^2)^2}{\gamma}\right)\mathbb{M}^2.\end{aligned}$$

Thus, we write

$$(\beta_h^2-\gamma)\|(\boldsymbol{u}_h,p_h)\|_{\mathrm{E}}^2 \lesssim \left(1+\frac{(1+\beta_h^2)^2}{\gamma}\right)\mathbb{M}^2.$$

Choosing γ to be equal to $\beta_h^2/2C$, being C the hidden constant in the above inequality, we finally arrive at

$$\|(\boldsymbol{u}_h,p_h)\|_{\mathrm{E}}^2 \lesssim \left(\frac{1}{\beta_h^2}+\frac{(1+\beta_h^2)^2}{\beta_h^4}\right)\mathbb{M}^2 \lesssim \frac{1}{\beta_h^2}\mathbb{M}^2,$$

i.e., $\|(\boldsymbol{u}_h,p_h)\|_{\mathrm{E}} \lesssim \alpha\mathbb{M}$ with $\alpha = O(\beta_h)$. The assertion follows from the definition of $\mathbb{M}$. □

Next, we show that [BNB(ii)] is valid, provided that the stabilization constant γ_v appearing in Definition 2.1 is chosen sufficiently large.

Proof. [Proof of [BNB(ii)]] Let $(\boldsymbol{u}_h,p_h)\in \mathbf{V}_h^\ell\times Q_h^m$ be such that

$$\mathcal{B}_h((\boldsymbol{v}_h,q_h);(\boldsymbol{u}_h,p_h))=0 \qquad \forall(\boldsymbol{v}_h,q_h)\in\mathbf{V}_h^\ell\times Q_h^m.$$

By taking $(\boldsymbol{v}_h,q_h)=(\boldsymbol{u}_h,p_h)$ and using (20), the couple $(\boldsymbol{u_h},p_h)$ satisfies

$$0 = a_h(\boldsymbol{u}_h,\boldsymbol{u}_h)+b_h(p_h,\boldsymbol{u}_h)-b_h(p_h,\boldsymbol{u}_h)+s_h(p_h,p_h).$$

Provided that the stabilization constant γ_v in Definition 2.1 is chosen sufficiently large, this implies

$$\|\boldsymbol{u}_h\|_{\mathbf{V}_h^\ell}^2+s_h(p_h,p_h)\lesssim 0,$$

whence $\boldsymbol{u}_h=\mathbf{0}$ follows.

Next, we prove that $p_h=0$. Thanks to the continuous *inf-sup* condition (12), we have

$$\|p_h\|_{L^2(\Omega)}^2 = -b(p_h,\boldsymbol{v}_{p_h})=\mathcal{B}_h((\boldsymbol{v}_{p_h},0);(\mathbf{0},p_h))=0,$$

whence the assertion follows. □

Summarizing the above computations, we eventually state the main result of the section, namely the well-posedness of problem (7).

Theorem 3.2 *Under the hypotheses of Proposition 3.1, [BNB(i)] and [BNB(ii)] are valid. Notably, the constant α in ([BNB(i)]) satisfies $\alpha = O(\beta_h)$, where β_h is defined as in Proposition 3.1. Therefore, thanks to Theorem 3.1, the discrete problem (7) is well-posed.*

The constant α in ([BNB(i)]) deteriorates as the polynomial degree grows. This is due to the use of the polynomial inverse estimates, which yield a discrete *inf-sup* constant depending on the polynomial degree.

4 Numerical evaluation of the generalized *inf-sup* constant

Denote the shape functions of $\boldsymbol{V}_h^\ell$ and Q_h^m by $\{\boldsymbol{\varphi}_i\}_{i=1}^{N_{\boldsymbol{u}}}$ and $\{\psi_j\}_{j=1}^{N_p}$, and the corresponding number of degrees of freedom by $N_{\boldsymbol{u}}$ and N_p, respectively. We write $\boldsymbol{u}_h=\sum_{j=1}^{N_{\boldsymbol{u}}}u_j\boldsymbol{\varphi}_i$ and

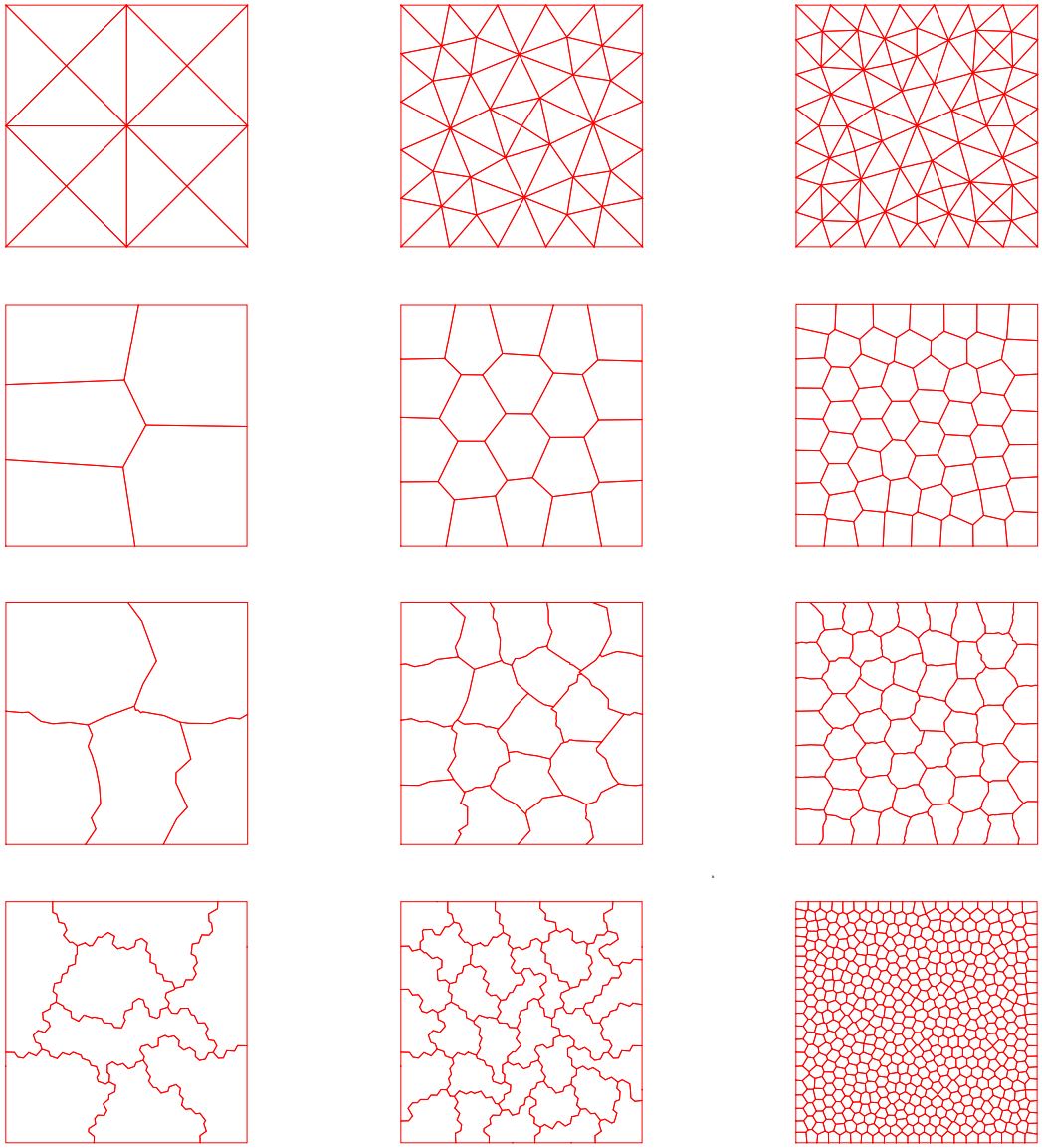

Figure 1: From top to bottom: triangular meshes with $N_{el} = 16, 68, 124$ (from left to right); regular polygonal meshes with $N_{el} = 5, 20, 60$ (from left to right); distorted polygonal meshes with $N_{el} = 5, 20, 60$ (from left to right); agglomerated polygonal meshes with $N_{el} = 8, 32, 512$ (from left to right).

$p_h = \sum_{j=1}^{N_p} p_j \psi_i$. The algebraic form of the stationary Stokes problem corresponding to the problem in (5) reads

$$\begin{bmatrix} A_h & B_h^T \\ B_h & -S_h \end{bmatrix} \begin{bmatrix} \boldsymbol{U} \\ \boldsymbol{P} \end{bmatrix} = \begin{bmatrix} \boldsymbol{F_h} \\ \boldsymbol{0} \end{bmatrix},$$

where $\boldsymbol{U} \in \mathbb{R}^{N_{\boldsymbol{u}}}$ and $\boldsymbol{P} \in \mathbb{R}^{N_{\boldsymbol{p}}}$ are the vectors collecting the expansion coefficients $\{u_j\}_j$ and $\{p_j\}_j$, respectively, whereas A_h, B_h, S_h, and $\boldsymbol{f_h}$ denote the matrix representations of the discrete bilinear forms in (4b)–(4d) and right-hand side in (5).

We recall that the discrete *inf-sup* condition given in Proposition 3.1 is given by

$$\sup_{\boldsymbol{0}\neq\boldsymbol{v}_h\in\mathbf{V}_h^\ell} \frac{b_h(q_h,\boldsymbol{v}_h)}{\|\boldsymbol{v}_h\|_{\mathbf{V}_h^\ell}} + \eta\,|q_h|_{\mathsf{J}} \geq \beta_h \|q_h\|_{L^2(\Omega)} \quad \forall q_h \in Q_h^m.$$

Here, we have added a parameter $\eta = \{0, 1\}$, so as to address numerically the case where no pressure stabilization is added in the discrete formulation. Introduce the generalized eigenvalue problem

$$G_h \boldsymbol{x} = \lambda T_h \boldsymbol{x}, \tag{23}$$

with $G_h = B_h A_h^{-1} B_h^T + \eta S_h$, $T_h = M$, where M is the mass matrix. We distinguish two cases:

- If $\eta = 1$ (pressure stabilization), the discrete *inf-sup* constant satisfies

  $$\beta_h \langle M\boldsymbol{q},\boldsymbol{q}\rangle^{1/2} \leq \langle B_h A_h^{-1} B_h^T \boldsymbol{q},\boldsymbol{q}\rangle^{1/2} + \langle S_h\boldsymbol{q},\boldsymbol{q}\rangle^{1/2} \quad \forall \boldsymbol{q} \in \mathbb{R}^{N_p}, \boldsymbol{q} \neq \boldsymbol{1}.$$

  By noting that $a + b \leq \left(\sqrt{a} + \sqrt{b}\right)^2 \leq 2a + 2b$, we have

  $$\begin{aligned} \beta_h^2 \langle M\boldsymbol{q},\boldsymbol{q}\rangle &\leq \langle B_h A_h^{-1} B_h^T \boldsymbol{q},\boldsymbol{q}\rangle + \langle S_h\boldsymbol{q},\boldsymbol{q}\rangle \\ &= \langle \left(B_h A_h^{-1} B_h^T + S_h\right)\boldsymbol{q},\boldsymbol{q}\rangle \qquad \forall \boldsymbol{q} \in \mathbb{R}^{N_p}, \boldsymbol{q} \neq 1 \end{aligned}$$

  and hence

  $$\beta_h^2 = \min_{\substack{\boldsymbol{q}\in\mathbb{R}^{N_p} \\ \boldsymbol{q}\neq\boldsymbol{1}}} \frac{\langle \left(B_h A_h^{-1} B_h^T + S_h\right)\boldsymbol{q},\boldsymbol{q}\rangle}{\langle M\boldsymbol{q},\boldsymbol{q}\rangle} = \min_{\substack{\boldsymbol{q}\in\mathbb{R}^{N_p} \\ \boldsymbol{q}\neq\boldsymbol{1}}} \frac{\langle G_h\boldsymbol{q},\boldsymbol{q}\rangle}{\langle T_h\boldsymbol{q},\boldsymbol{q}\rangle}.$$

- If $\eta = 0$ (no pressure stabilization), the discrete *inf-sup* constant satisfies

$$\begin{aligned}\beta_h &= \min_{\substack{\boldsymbol{q}\in\mathbb{R}^{N_p}\\ \boldsymbol{q}\neq\boldsymbol{1}}} \max_{\substack{\boldsymbol{v}\in\mathbb{R}^{N_{\boldsymbol{u}}}\\ \boldsymbol{v}\neq\boldsymbol{0}}} \frac{|\langle \boldsymbol{q}, B_h\boldsymbol{v}\rangle|}{\langle A_h\boldsymbol{v},\boldsymbol{v}\rangle^{1/2}\langle M\boldsymbol{q},\boldsymbol{q}\rangle^{1/2}} \\ &= \min_{\substack{\boldsymbol{q}\in\mathbb{R}^{N_p}\\ \boldsymbol{q}\neq\boldsymbol{1}}} \frac{1}{\langle M\boldsymbol{q},\boldsymbol{q}\rangle^{1/2}} \max_{\substack{\boldsymbol{w}\in\mathbb{R}^{N_{\boldsymbol{u}}}\\ \boldsymbol{w}=A_h^{1/2}\boldsymbol{v}\neq\boldsymbol{0}}} \frac{\left|\langle \boldsymbol{q}, B_hA_h^{-1/2}\boldsymbol{w}\rangle\right|}{\langle \boldsymbol{w},\boldsymbol{w}\rangle^{1/2}} \\ &= \min_{\substack{\boldsymbol{q}\in\mathbb{R}^{N_p}\\ \boldsymbol{q}\neq\boldsymbol{1}}} \frac{1}{\langle M\boldsymbol{q},\boldsymbol{q}\rangle^{1/2}} \max_{\substack{\boldsymbol{w}\in\mathbb{R}^{N_{\boldsymbol{u}}}\\ \boldsymbol{w}\neq\boldsymbol{0}}} \frac{\left|\langle A_h^{-1/2}B_h^T\boldsymbol{q}, \boldsymbol{w}\rangle\right|}{\langle \boldsymbol{w},\boldsymbol{w}\rangle^{1/2}}.\end{aligned}$$

  By noting that the maximum is realized for $\boldsymbol{w} = A_h^{-1/2}B_h^T\boldsymbol{q}$, we have

$$\begin{aligned}\beta_h^2 &= \min_{\substack{\boldsymbol{q}\in\mathbb{R}^{N_p}\\ \boldsymbol{q}\neq\boldsymbol{1}}} \frac{\langle A_h^{-1/2}B_h^T\boldsymbol{q}, A_h^{-1/2}B_h^T\boldsymbol{q}\rangle}{\langle M\boldsymbol{q},\boldsymbol{q}\rangle} = \min_{\substack{\boldsymbol{q}\in\mathbb{R}^{N_p}\\ \boldsymbol{q}\neq\boldsymbol{1}}} \frac{\langle B_hA_h^{-1}B_h^T\boldsymbol{q},\boldsymbol{q}\rangle}{\langle M\boldsymbol{q},\boldsymbol{q}\rangle} \\ &= \min_{\substack{\boldsymbol{q}\in\mathbb{R}^{N_p}\\ \boldsymbol{q}\neq\boldsymbol{1}}} \frac{\langle G_h\boldsymbol{q},\boldsymbol{q}\rangle}{\langle T_h\boldsymbol{q},\boldsymbol{q}\rangle}.\end{aligned}$$

By solving the discrete eigenvalue problem in equation (23), we have that

$$\beta_h \approx \min_{\lambda_i>0} \sqrt{\lambda_i}.$$

To estimate numerically β_h, we consider the Stokes problem on the unit square domain $\Omega = (0,1)^2$. We computed β_h on several sequences of meshes, namely triangular, regular, distorted, and agglomerated polygonal meshes; see Figure 1 for an illustrative example of the considered grids. The regular polygonal meshes have been generated via `PolyMesher` [53], while the distorted polygonal ones are generated starting from a regular grid and randomly adding grid nodes on the edges to obtain elements with a large number of possibly degenerating edges. The resulting elements may be non-convex. The sequence of agglomerated polygonal meshes are generated by agglomerating elements starting from an initial Voronoi tessellation; see the last row of Figure 1. To solve the generalized eigenvalue problem (23), we employ the `eigs` command of Matlab.

We first investigate the behavior of β_h for fixed polynomial approximation orders for the velocity and the pressure and varying the mesh size. In Figures 2 and 3, we report the computed values of β_h as a function of the mesh size h for different mesh configurations and different choices of the discrete velocity and pressure spaces $\mathcal{P}^{m+k}-\mathcal{P}^m$, $k = 0,1,2,3,4$. In the stabilized cases $\eta = 1$, the constant β_h is uniformly bounded from 0 independently of the mesh size. This is in agreement with the result shown in Proposition 3.1. Furthermore,

as predicted in Proposition 3.1, β_h depends on m for all the considered mesh configurations, at least when $m = \ell$. From the numerical computations obtained in the no pressure stabilization cases $\eta = 0$ with $k = 1, 2, 3, 4$, we draw the following conclusions: *(i)* β_h is independent of h for all the considered mesh configurations except for agglomerated meshes, where we can detect a mild dependence; *(ii)* the dependence of β_h on the velocity and pressure polynomial approximation degrees is stronger than in the stabilized case.

Next, we investigate the behavior of β_h by varying the polynomial approximation orders for the velocity and the pressure spaces, and fixing the computational mesh. In Figure 4, we report the computed value of β_h as a function of the polynomial approximation degree m for different choices of the velocity and pressure spaces $\mathcal{P}^{m+k} - \mathcal{P}^m$, $k = 0, 1, 2, 3, 4$. We set the parameter $\eta = 1$ for $k = 0, 1, 2$, and $\eta = 0$ for $k = 1, 2, 3, 4$. When $\eta = 1$, we obtain the following results. For $k = 0$, i.e., $\ell = m$, the dependence of β_h is in agreement with Proposition 3.1: the constant β_h deteriorates as m grows. Nevertheless, the estimate in Proposition 3.1 is slightly suboptimal by a factor of $m^{-1/2}$, as our numerical computations suggest that $\beta_h = O(m^{-1/2})$ for all the considered mesh configurations. For $k = 1, 2$, on triangular and regular polygonal meshes, β_h looks independent of m, while mildly depends on m on irregular and agglomerated polygonal meshes. From the numerical computations obtained in the no pressure stabilization cases $\eta = 0$, we draw the following conclusions: *(i)* on regular polygonal meshes, β_h is independent of m for all the considered velocity-pressure pairs $\mathcal{P}^{m+k} - \mathcal{P}^m$, $k = 1, 2, 3, 4$; *(ii)* on irregular and agglomerated polygonal meshes, the behavior of β_h is less clear and we detect a mild dependence on m. By comparing the cases $\mathcal{P}^{m+k} - \mathcal{P}^m$, $k = 1, 2$ with and without pressure stabilization, at least for the agglomerated polygonal meshes, the dependence of β_h on m is milder for the case $\eta = 1$.

Moreover, we study the behaviour of β_h in the case of degenerate edges, i.e., when the number of the edges of a polygon with fixed size increases and the size of the edges tends to zero. In particular, we consider an initial triangular mesh with a uniform mesh size; see Figure 5 (left). Starting from this grid, we generate a sequence of meshes by halving recursively the edges of the element at the center of the mesh, leading to a polygon with an increasing number of edges; see Figure 5 (middle and right). We indicate the number of the edges of the polygon with $\#edges$. In Figure 6, we report the values of β_h as a function of $\#edges$ for different choices of the discrete velocity and pressure spaces $\mathcal{P}^{m+k} - \mathcal{P}^m$, $k = 0, 1, 2$, with ($\eta = 1$) and without ($\eta = 0$) pressure stabilization. The computed numerical *inf-sup* constant β_h seems to be independent of the size of the edges for any choice of k and the pressure stabilization term. This indicates that Assumption 3.2 in Proposition 3.1 may be relaxed; see Remark 3.3.

Finally, we consider a sequence of grids that mimics fluid meshes typically appearing in fluid-structure interaction applications; see Section 7 below. These grids are generated as follows: first, consider a uniform regular triangular mesh of a square domain; next, carve the domain out and get a hole inside it. For example, this hole may represent a structure domain immersed in a fluid one. In the proximity of the hole, the resulting mesh presents polygonal elements that may be non-convex, of arbitrary size and of anisotropic shape.

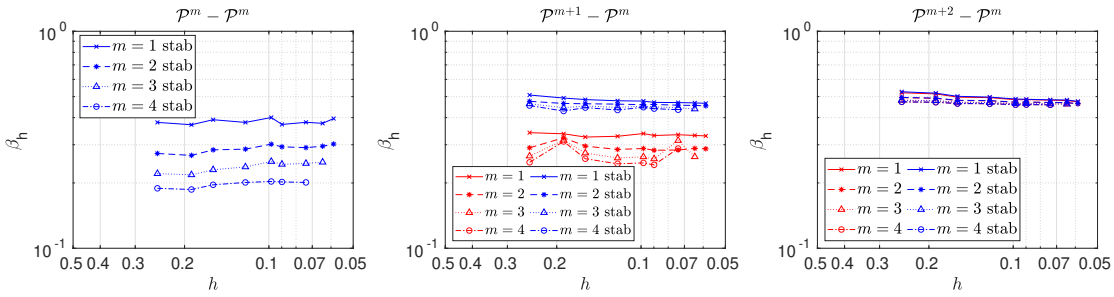

(a) Triangular grids

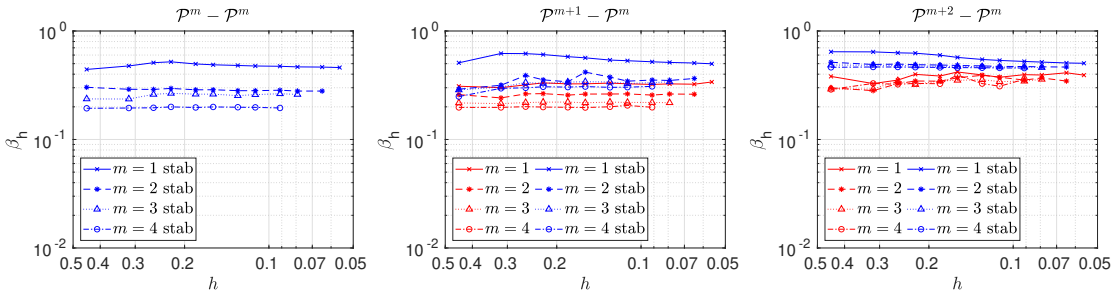

(b) Regular polygonal meshes

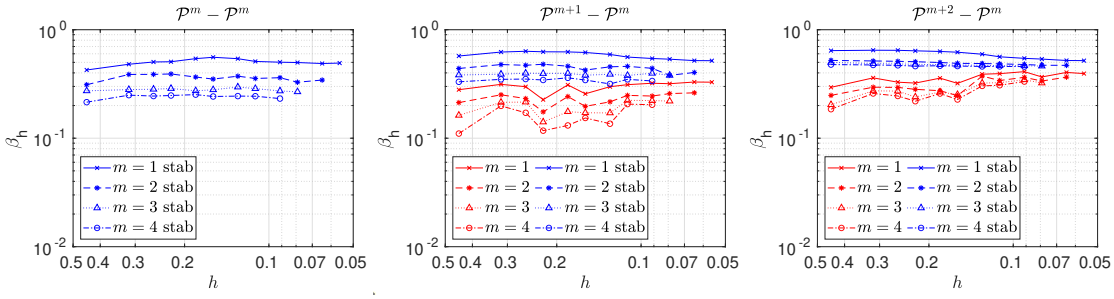

(c) Distorted polygonal meshes

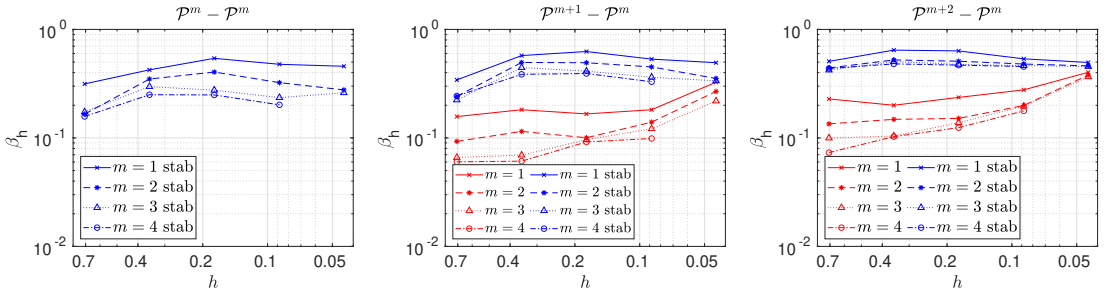

(d) Agglomerated polygonal meshes

Figure 2: Values of β_h as function of the mesh size h for different choices of the polynomial degree for the discrete velocity and pressure spaces $\mathcal{P}^{m+k} - \mathcal{P}^m$, computed solving the generalized eigenvalue problem (23). From left to right: $\mathcal{P}^m - \mathcal{P}^m$, $\mathcal{P}^{m+1} - \mathcal{P}^m$, $\mathcal{P}^{m+2} - \mathcal{P}^m$. The parameter $\eta = 1$ for $k = 0, 1, 2$ (blue lines), and $\eta = 0$ for $k = 1, 2$ (red lines).

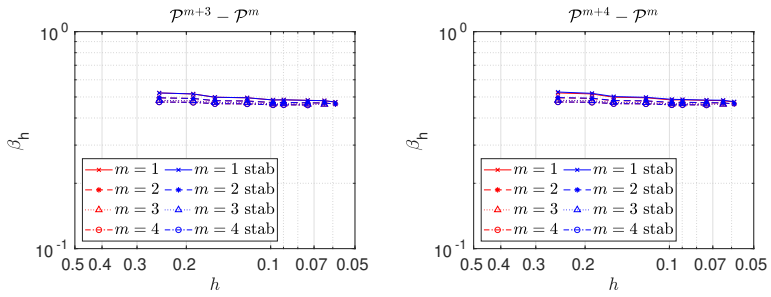

(a) Triangular grids

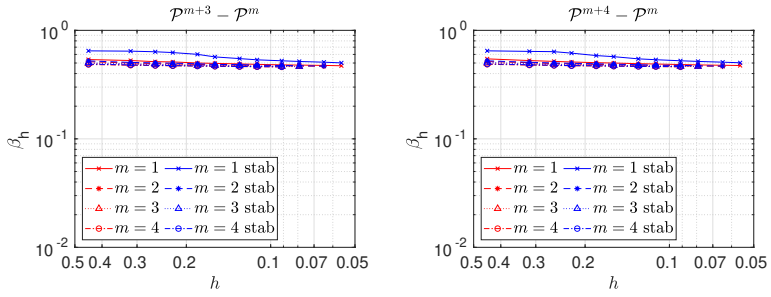

(b) Regular polygonal meshes

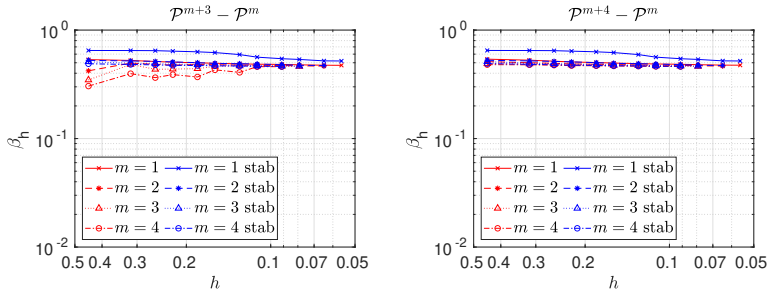

(c) Distorted polygonal meshes

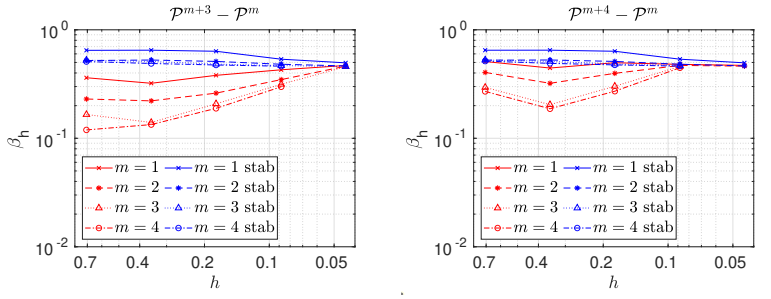

(d) Agglomerated polygonal meshes

Figure 3: Values of β_h as function of the mesh size h for different choices of the polynomial degree for the discrete velocity and pressure spaces $\mathcal{P}^{m+k} - \mathcal{P}^m$, computed solving the generalized eigenvalue problem (23). From left to right: $\mathcal{P}^{m+3} - \mathcal{P}^m$, $\mathcal{P}^{m+4} - \mathcal{P}^m$. The parameter $\eta = 1$ (blue lines) and $\eta = 0$ (red lines).

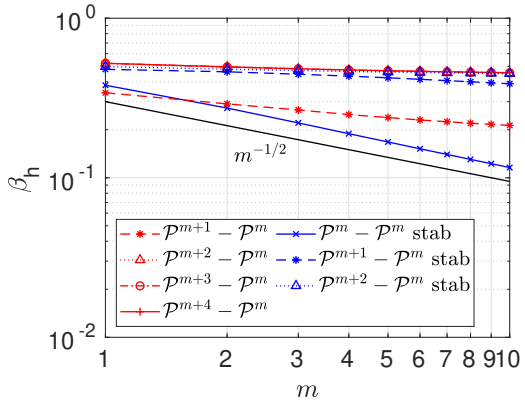

(a) Triangular grids ($N_{el} = 16$)

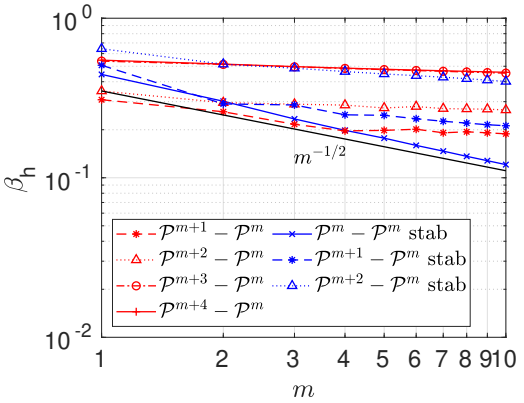

(b) Regular polygonal meshes ($N_{el} = 5$)

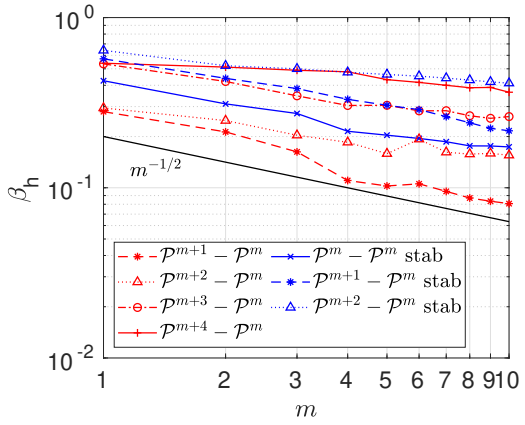

(c) Distorted polygonal meshes ($N_{el} = 5$)

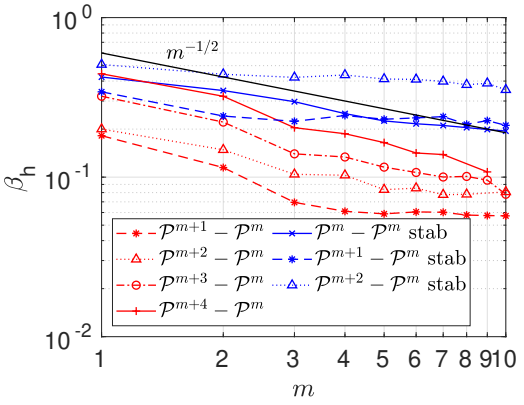

(d) Agglomerated polygonal meshes ($N_{el} = 8$)

Figure 4: Values of β_h as function of the polynomial degree for different choices of the velocity and pressure spaces $\mathcal{P}^{m+k} - \mathcal{P}^m$, $k = 0, 1, 2, 3, 4$ computed solving the generalized eigenvalue problem (23). The parameter $\eta = 1$ if $k = 0, 1, 2$ (blue lines), and $\eta = 0$ if $k = 1, 2, 3, 4$ (red lines).

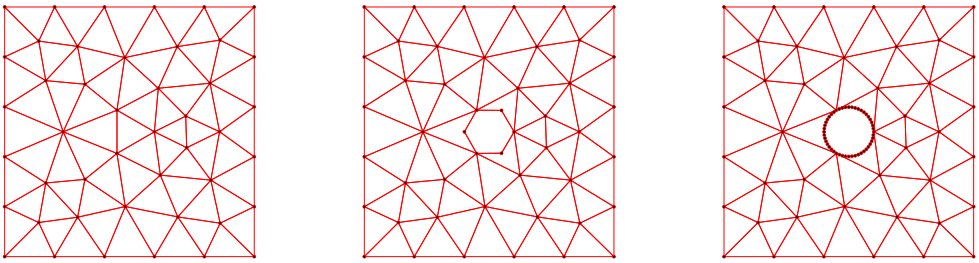

Figure 5: Meshes obtained with a recursive splitting of the edges of the element at the center. From left to right: initial triangular meshes with $\#edges = 3$; mesh at the first iteration with $\#edges = 6$; mesh at the fourth iteration with $\#edges = 48$.

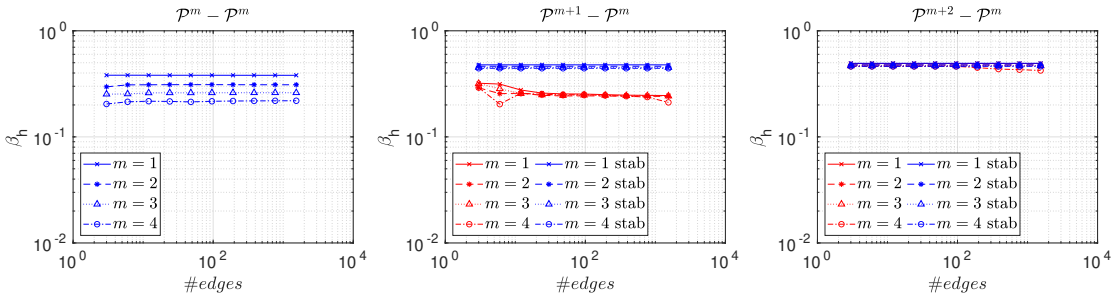

Figure 6: Values of β_h as function of the number of edges $\#edges$ for different choices of the polynomial degree for the discrete velocity and pressure spaces $\mathcal{P}^{m+k} - \mathcal{P}^m$, computed solving the generalized eigenvalue problem (23). From left to right: $\mathcal{P}^m - \mathcal{P}^m$, $\mathcal{P}^{m+1} - \mathcal{P}^m$, $\mathcal{P}^{m+2} - \mathcal{P}^m$. The parameter $\eta = 1$ for $k = 0, 1, 2$ (blue lines), and $\eta = 0$ for $k = 1, 2$ (red lines).

We consider a slender rectangular hole placed in the center of the square domain that rotates around its center of mass, see Figure 7, and we study the behaviour of the discrete *inf-sup* constant β_h by varying the angle of rotation θ of the hole. In Figure 8, we plot the value of the discrete *inf-sup* constant as a function of the angle θ for different choices of the discrete velocity and pressure spaces $\mathcal{P}^{m+k} - \mathcal{P}^m$, $k = 0, 1, 2$, $m = 1, 2$, with and without the pressure stabilization term. The presence of small or anisotropic elements only slightly deteriorates the constant β_h for the nonstabilized case ($\eta = 0$), while they seem irrelevant for the stabilized case ($\eta = 1$).

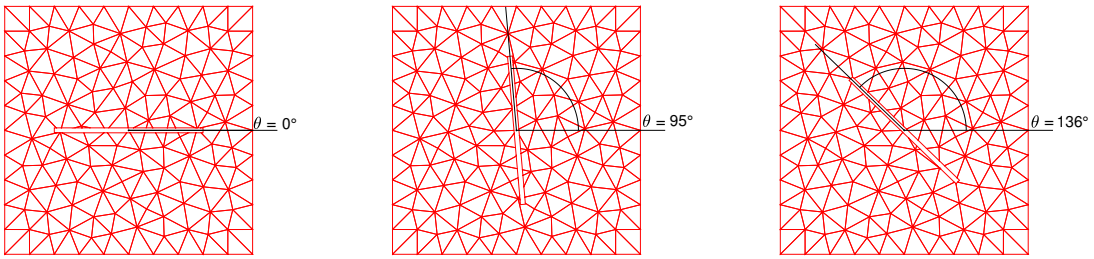

Figure 7: Polygonal meshes obtained by rotating the hole placed in the center of the initial triangular mesh. Small or anisotropic elements appear. From left to right: polygonal mesh obtained for $\theta = 0°$; polygonal mesh obtained for $\theta = 95°$; polygonal mesh obtained for $\theta = 136°$.

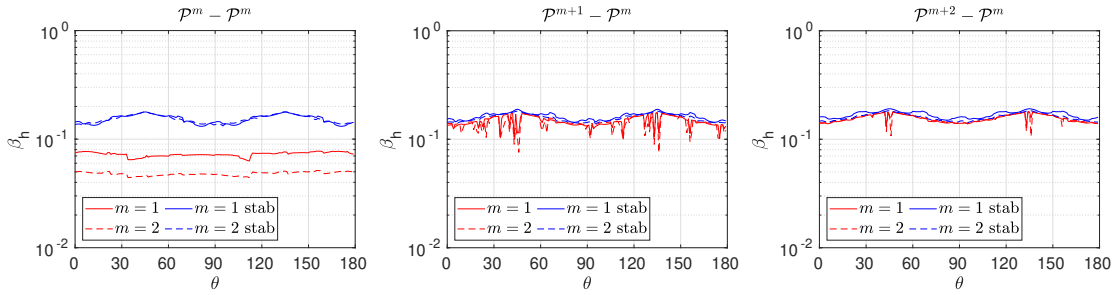

Figure 8: Values of β_h as function of the angle of rotation θ for different choices of the polynomial degree for the discrete velocity and pressure spaces $\mathcal{P}^{m+k} - \mathcal{P}^m$, computed solving the generalized eigenvalue problem (23). From left to right: $\mathcal{P}^m - \mathcal{P}^m$, $\mathcal{P}^{m+1} - \mathcal{P}^m$, $\mathcal{P}^{m+2} - \mathcal{P}^m$. The parameter $\eta = 1$ (blue lines) and $\eta = 0$ (red lines).

5 A priori error estimates for the stationary Stokes problem

Introduce the spaces $\mathcal{X} = \mathbf{V}_h^\ell \cap [H^2(\Omega)]^d$ and $\mathcal{M} = Q_h^m \cap H^1(\Omega)$ for the velocity and pressure, respectively. For all $(\boldsymbol{u}, p), (\boldsymbol{v}, q) \in \mathcal{X} \times \mathcal{M}$, we consider the discrete bilinear

form $\mathcal{B}_h$ introduced in equation (6).

Define $\|(\cdot,\cdot)\|_{\mathcal{X}\times\mathcal{M}}$ as the energy norm defined on the pair of spaces $\mathcal{X}\times\mathcal{M}$. In particular, we fix

$$\|(\boldsymbol{v}_h, q_h)\|^2_{\mathcal{X}\times\mathcal{M}} = \|\boldsymbol{v}_h\|^2_{\mathbf{V}_h^\ell} + \|q_h\|^2_{Q_h^m}.$$

We now state the main result of the section.

Theorem 5.1 (Abstract error estimate) *Let $(\boldsymbol{u},p)\in\mathcal{X}\times\mathcal{M}$ and $(\boldsymbol{u}_h,p_h)\in\mathbf{V}_h^\ell\times Q_h^m$ be the solutions to (2) and (7), respectively, and Assumptions 3.1 and 3.2 be valid. Recalling that the bilinear form $\mathcal{B}_h(\cdot,\cdot)$ is stable and bounded with constants C^* and C_*, the following error estimate is valid:*

$$\|(\boldsymbol{u}-\boldsymbol{u}_h, p-p_h)\|_{\mathcal{X}\times\mathcal{M}} \leq \left(1+\frac{C_*}{C^*}\right) \inf_{(\boldsymbol{v}_h,q_h)\in\mathbf{V}_h^\ell\times Q_h^m} \|(\boldsymbol{u}-\boldsymbol{v}_h, p-q_h)\|_{\mathcal{X}\times\mathcal{M}}. \tag{24}$$

Proof. For all $(\boldsymbol{v}_h,q_h)\in\mathbf{V}_h^\ell\times Q_h^m$, we apply the triangle inequality and get

$$\|(\boldsymbol{u}-\boldsymbol{u}_h, p-p_h)\|_{\mathcal{X}\times\mathcal{M}} \leq \|(\boldsymbol{u}-\boldsymbol{v}_h, p-q_h)\|_{\mathcal{X}\times\mathcal{M}} + \|(\boldsymbol{v}_h-\boldsymbol{u}_h, q_h-p_h)\|_{\mathcal{X}\times\mathcal{M}}. \tag{25}$$

We have the following Galerkin orthogonality property. Given $(\boldsymbol{u},p)$ and $(\boldsymbol{u}_h,p_h)$ the solutions to the continuous and discrete Stokes problem, respectively, we can write

$$\mathcal{B}_h((\boldsymbol{u}-\boldsymbol{u_h}, p-p_h),(\boldsymbol{w}_h,r_h)) = 0 \qquad \forall(\boldsymbol{w}_h,r_h)\in\boldsymbol{V}_h^\ell\times Q_h^m. \tag{26}$$

The main tool used in proving (26) is the extra smoothness required on the continuous pressure p, whence the jump terms involving it disappear.

Using the coercivity, the Galerkin orthogonality (26), and the continuity of the form $\mathcal{B}_h$, we can show an upper bound on the second term of the previous inequality as follows:

$$\begin{aligned}
\|(\boldsymbol{v}_h-\boldsymbol{u}_h, q_h-p_h)\|_{\mathcal{X}\times\mathcal{M}} &\leq \frac{1}{C^*} \sup_{(\boldsymbol{w}_h,r_h)\in\mathbf{V}_h^\ell\times Q_h^m} \frac{\mathcal{B}_h((\boldsymbol{v}_h-\boldsymbol{u}_h, q_h-p_h),(\boldsymbol{w}_h,r_h))}{\|(\boldsymbol{w}_h,r_h)\|_{\mathcal{X}\times\mathcal{M}}} \\
&= \frac{1}{C^*} \sup_{(\boldsymbol{w}_h,r_h)\in\mathbf{V}_h^\ell\times Q_h^m} \frac{\mathcal{B}_h((\boldsymbol{v}_h-\boldsymbol{u}, q_h-p),(\boldsymbol{w}_h,r_h))}{\|(\boldsymbol{w}_h,r_h)\|_{\mathcal{X}\times\mathcal{M}}} \\
&\quad + \frac{1}{C^*} \sup_{(\boldsymbol{w}_h,r_h)\in\mathbf{V}_h^\ell\times Q_h^m} \frac{\mathcal{B}_h((\boldsymbol{u}-\boldsymbol{u}_h, p-p_h),(\boldsymbol{w}_h,r_h))}{\|(\boldsymbol{w}_h,r_h)\|_{\mathcal{X}\times\mathcal{M}}} \\
&\leq \frac{C_*}{C^*}\|(\boldsymbol{u}-\boldsymbol{v}_h, p-q_h)\|_{\mathcal{X}\times\mathcal{M}}
\end{aligned} \tag{27}$$

Inserting the inequality (27) into (25), the assertion follows. □

Finally, by employing the approximation results reported in Section 3 with Theorem 5.1, we show the *hp*-version a priori error estimate for the discrete Stokes problem in (7).

Corollary 5.1 (Convergence rate in the energy norm) *Let $\mathcal{T}_h$ be a polytopic mesh and $\mathcal{T}_h^\#$ be the corresponding covering satisfying Definition 3.1. Moreover, let Assumptions 3.1 and 3.2, and the hypotheses of Theorem 5.1 be valid. Finally assume that $\ell\geq$*

$m-1$. *If, for any* $K \in \mathcal{T}_h$, $(\boldsymbol{u}, p)|_K \in H^r(K) \times H^{r-1}(K)$, *with* $r > 1 + d/2$, *such that for any* $\mathcal{K} \in \mathcal{T}_h^{\#}$, $K \subset \mathcal{K}$, $(\mathcal{E}\boldsymbol{u}, \mathcal{E}p)|_{\mathcal{K}} \in H^r(\mathcal{K}) \times H^{r-1}(\mathcal{K})$, *then*

$$\|(\boldsymbol{u} - \boldsymbol{u}_h, p - p_h)\|_{\mathcal{X}\times\mathcal{M}} \lesssim \sum_{K\in\mathcal{T}_h} \frac{h_K^{s-1}}{\ell^{r-3/2}} \left(\|\mathcal{E}\boldsymbol{u}\|_{H^r(\mathcal{K})} + \|\mathcal{E}p\|_{H^{r-1}(\mathcal{K})} \right),$$

where $s = \min\{\ell + 1, m + 2, r\}$ *and the hidden positive constant is independent of the discretization parameters.*

Proof. By considering equation (24), we set

$$\mathcal{I} = \inf_{(\boldsymbol{v}_h, q_h) \in \mathbf{V}_h^\ell \times Q_h^m} \|(\boldsymbol{u} - \boldsymbol{v}_h, p - q_h)\|_{\mathcal{X}\times\mathcal{M}}.$$

Recall that Π^ℓ denotes the best polynomial approximant introduced in Lemma 3.2. With an abuse of notation, we shall use the same symbol for scalar, vector, and tensor approximants. We have

$$\begin{aligned}
\mathcal{I}^2 &= \inf_{(\boldsymbol{v}_h, q_h) \in \mathbf{V}_h^\ell \times Q_h^m} \|(\boldsymbol{u} - \boldsymbol{v}_h, p - q_h)\|^2_{\mathcal{X}\times\mathcal{M}} \leq \|(\boldsymbol{u} - \Pi^\ell \boldsymbol{u}, p - \Pi^m p)\|^2_{\mathcal{X}\times\mathcal{M}}, \\
&\leq \underbrace{\sum_{K\in\mathcal{T}_h} \|\mu^{1/2} \nabla (\boldsymbol{u} - \Pi^\ell \boldsymbol{u})\|^2_{L^2(K)} + \sum_{F\in\mathcal{F}_h} \|\sigma_v^{1/2} [\![\boldsymbol{u} - \Pi^\ell \boldsymbol{u}]\!]\|^2_{L^2(F)}}_{\text{(A)}} \\
&\quad + \underbrace{\sum_{K\in\mathcal{T}_h} \|p - \Pi^m p\|^2_{L^2(K)} + \sum_{F\in\mathcal{F}_h} \|\sigma_p^{1/2} [\![p - \Pi^m p]\!]\|^2_{L^2(F)}}_{\text{(B)}}.
\end{aligned}$$

By using Lemmata 3.2 and 3.1, Assumption **A.3**, and $\ell \geq m-1$, we can prove the following bounds on the terms (A) and (B):

$$\begin{aligned}
\text{(A)} &\lesssim \sum_{K\in\mathcal{T}_h} \mu \frac{h_K^{2(s_u-1)}}{\ell^{2(r-1)}} \|\mathcal{E}\boldsymbol{u}\|^2_{H^r(\mathcal{K})} + \sum_{K\in\mathcal{T}_h} (\max_{F\subset\partial K} \sigma_v) \frac{h_K^{2(s_u-1/2)}}{\ell^{2(r-1/2)}} \|\mathcal{E}\boldsymbol{u}\|^2_{H^r(\mathcal{K})} \\
&\lesssim \sum_{K\in\mathcal{T}_h} \frac{h_K^{2(s_u-1)}}{\ell^{2(r-1)}} \|\mathcal{E}\boldsymbol{u}\|^2_{H^r(\mathcal{K})} + \sum_{K\in\mathcal{T}_h} \frac{\ell^2}{h_K} \frac{h_K^{2(s_u-1/2)}}{\ell^{2(r-1/2)}} \|\mathcal{E}\boldsymbol{u}\|^2_{H^r(\mathcal{K})} \\
&\lesssim \sum_{K\in\mathcal{T}_h} \frac{h_K^{2(s_u-1)}}{\ell^{2(r-3/2)}} \|\mathcal{E}\boldsymbol{u}\|^2_{H^r(\mathcal{K})},
\end{aligned}$$

and

$$\begin{aligned}
\text{(B)} &\lesssim \sum_{K\in\mathcal{T}_h} \frac{h_K^{2s_p}}{m^{2(r-1)}} \|\mathcal{E}p\|^2_{H^{r-1}(\mathcal{K})} + \sum_{K\in\mathcal{T}_h} (\max_{F\subset\partial K} \sigma_p) \frac{h_K^{2(s_p-1/2)}}{m^{2(r-3/2)}} \|\mathcal{E}p\|^2_{H^{r-1}(\mathcal{K})} \\
&\lesssim \sum_{K\in\mathcal{T}_h} \frac{h_K^{2s_p}}{m^{2(r-1)}} \|\mathcal{E}p\|^2_{H^{r-1}(\mathcal{K})} + \sum_{K\in\mathcal{T}_h} \frac{h_K}{m} \frac{h_K^{2(s_p-1/2)}}{m^{2(r-3/2)}} \|\mathcal{E}p\|^2_{H^{r-1}(\mathcal{K})} \\
&\lesssim \sum_{K\in\mathcal{T}_h} \frac{h_K^{2s_p}}{m^{2(r-1)}} \|\mathcal{E}p\|^2_{H^{r-1}(\mathcal{K})},
\end{aligned}$$

where $s_u = \min\{\ell+1, r\}$ and $s_p = \min\{m+1, r-1\}$.

Finally, we obtain, $s = \min\{\ell+1, m+2, r\}$,

$$\mathcal{I}^2 \lesssim \sum_{K\in\mathcal{T}_h} \frac{h_K^{2(s-1)}}{\ell^{2(r-3/2)}} \left(\|\mathcal{E}\boldsymbol{u}\|_{H^r(\mathcal{K})} + \|\mathcal{E}p\|_{H^{r-1}(\mathcal{K})} \right)^2 .$$

By inserting the bound on $\mathcal{I}$ into (24), the assertion follows. □

Remark 5.1 *The estimate of Corollary 5.1 is suboptimal in terms of half a polynomial order also due to the presence of the coercivity constant $C^* = C^*(\beta_h)$, where β_h is the discrete generalized inf-sup constant introduced in Proposition 3.1.*

Remark 5.2 *By assuming $h \simeq h_K$, for any $K \in \mathcal{T}_h$, and uniform regularity of the solution, the estimate in Corollary 5.1 becomes:*

$$\|(\boldsymbol{u}-\boldsymbol{u}_h, p-p_h)\|_{\mathcal{X}\times\mathcal{M}} \lesssim \frac{h^{s-1}}{\ell^{r-3/2}} \left(\|\mathcal{E}\boldsymbol{u}\|_{H^r(\cup_{K\in\mathcal{T}_h}\mathcal{K})} + \|\mathcal{E}p\|_{H^{r-1}(\cup_{K\in\mathcal{T}_h}\mathcal{K})} \right).$$

where $s = \min\{\ell+1, m+2, r\}$ and the hidden positive constant is independent of the discretization parameters.

Remark 5.3 *We can also prove a priori error estimates by setting minimal regularity $\mathcal{X} = \mathbf{V}_h^\ell \cap H_0^1(\Omega)$ and $\mathcal{M} = Q_h^m$ for the velocity and pressure, respectively. This requires to introduce a nonconsistent formulation, modify the bilinear form in equation (6), and consider the residual term of the Strang's lemma in Theorem 5.1.*

6 An application: PolyDG for FSI problems

In this section, we introduce a continuos FSI problem and its PolyDG discretization, with the aim of further exploring the stability properties of the PolyDG discretization of the Stokes problem and their impact on the approximation of related differential problems; see Section 7 below.

Let $\Omega \subset \mathbb{R}^d$ and $\Omega_s \subset \mathbb{R}^d$, $d = 2, 3$, be two polygonal/polyhedral domains. In Ω, we consider an incompressible Newtonian fluid with density ρ and dynamic viscosity μ, where $\boldsymbol{u}$ and p are the fluid velocity and pressure, while in Ω_s we consider a linear elastic material with density ρ_s, Young's modulus E, and Poisson's ratio ν, where $\boldsymbol{d}$ is the solid displacement.

In what follows, we denote by Σ the fluid-structure interface and by $\boldsymbol{n}$ its normal vector pointing outwards of Ω_s. We indicate with $\partial\Omega$ and $\partial\Omega_s$ the outer boundary of the fluid and solid domain, respectively. The domains may change in time.

The fluid-structure interaction problem reads as follows: for any $t \in (0, T]$, with $T > 0$, find the fluid velocity $\boldsymbol{u} = \boldsymbol{u}(t)$, the fluid pressure $p = p(t)$, and the solid displacement

$\boldsymbol{d} = \boldsymbol{d}(t)$, such that

$$
\begin{aligned}
&\rho \partial_t \boldsymbol{u} - \nabla \cdot \boldsymbol{T}_f(\boldsymbol{u}, p) = \boldsymbol{f} && \text{in } \Omega(t),\\
&\nabla \cdot \boldsymbol{u} = 0 && \text{in } \Omega(t),\\
&\boldsymbol{u} = 0 && \text{on } \partial\Omega,\\
&\boldsymbol{u} = \partial_t \boldsymbol{d} && \text{on } \Sigma(t),\\
&\boldsymbol{T}_f(\boldsymbol{u}, p)\boldsymbol{n} = \boldsymbol{T}_s(\boldsymbol{d})\boldsymbol{n} && \text{on } \Sigma(t),\\
&\rho_s \partial_{tt} \widehat{\boldsymbol{d}} - \nabla \cdot \widehat{\boldsymbol{T}}_s(\boldsymbol{d}) = \boldsymbol{f}_s && \text{in } \widehat{\Omega}_s,\\
&\widehat{\boldsymbol{d}} = \boldsymbol{0} && \text{on } \partial\widehat{\Omega}_s,
\end{aligned}
$$

where $\boldsymbol{T}_f(\boldsymbol{u}, p) = 2\mu \boldsymbol{D}(\boldsymbol{u}) - p\boldsymbol{I}$ is the fluid Cauchy stress tensor and $\widehat{\boldsymbol{T}}_s(\boldsymbol{d}) = 2\mu_s \boldsymbol{D}(\widehat{\boldsymbol{d}}) + \lambda_s \nabla \cdot \widehat{\boldsymbol{d}} \boldsymbol{I}$ is the solid first Piola-Kirchhoff stress tensor, with $\boldsymbol{D}(\boldsymbol{w}) = 1/2 \left(\nabla \boldsymbol{w} + \nabla^T \boldsymbol{w}\right)$ and $\lambda_s = \frac{E\nu}{(1+\nu)(1-2\nu)}$, $\mu_s = \frac{E}{2(1+\nu)}$ are the Lamé parameters.

The structure problem is written in the reference configuration $\widehat{\Omega}_s = \Omega_s(t = 0)$, and all the related quantities are indicated with the $\widehat{\cdot}$ notation.

Given the time discretization parameter $\Delta t > 0$, we indicate with $t^n = n\Delta t$, $n \geq 0$, the n-th time step and indicate the approximation of the unknown u at time t^n by u^n. We introduce the fluid and solid meshes $\mathcal{T}_{f,h}^n$ and $\mathcal{T}_{s,h}^n$, respectively, of the fluid and solid domains $\Omega(t^n)$ and $\Omega_s(t^n)$, respectively. We denote the $(d-1)$-dimensional faces at time t^n of the fluid and solid meshes by $\mathcal{F}_{f,h}^n$ and $\mathcal{F}_{s,h}^n$, respectively, except the set of faces composing the fluid-structure interface Σ at time t^n, which are denoted by $\mathcal{F}_{\Sigma,h}^n$. Finally, $\boldsymbol{V}_h^{\ell,n}$ and $Q_h^{m,n}$ are the fluid velocity and pressure spaces evaluated at time t^n, defined as

$$
\begin{aligned}
\boldsymbol{V}_h^{\ell,n} &= \{\boldsymbol{v} \in [L^2(\Omega(t^n))]^d : \boldsymbol{v}|_K \in [\mathcal{P}^\ell(K)]^d \ \forall K \in \mathcal{T}_{f,h}^n\},\\
Q_h^{m,n} &= \{q \in L_0^2(\Omega(t^n)) : q|_K \in \mathcal{P}^m(K) \ \forall K \in \mathcal{T}_{f,h}^n\}.
\end{aligned}
$$

The solid displacement space $\boldsymbol{W}_h^\ell$ evaluated in the reference configuration is defined as

$$
\boldsymbol{W}_h^\ell = \{\boldsymbol{w} \in [L^2(\widehat{\Omega}_s)]^d : \boldsymbol{w}|_K \in [\mathcal{P}^\ell(K)]^d \ \forall K \in \widehat{\mathcal{T}}_{s,h}\}.
$$

We have assumed that the spatial polynomial order ℓ is the same for both the fluid velocity and the solid displacement.

Given $r \in \mathbb{N}^+$, we apply a Backward Difference Formula (BDF) scheme [40] of order r both for the fluid and the solid subproblems. We indicate the coefficients appearing in the approximation of the first and second order time derivatives with ξ_i and ζ_i, $i = 0, \ldots, r$, respectively.

Define

$$
\begin{aligned}
A_{f,h}^n\left(\boldsymbol{u}_h^n, p_h^n; \boldsymbol{v}_h, q_h\right) = \rho \left(\frac{\xi_0}{\Delta t}\boldsymbol{u}_h^n, \boldsymbol{v}_h\right)_{\Omega^n} &+ a_{f,h}^n\left(\boldsymbol{u}_h^n, \boldsymbol{v}_h\right) + b_h^n\left(p_h^n, \boldsymbol{v}_h\right) - b_h^n\left(q_h, \boldsymbol{u}_h^n\right)\\
&+ s_h^n\left(p_h^n, q_h\right);
\end{aligned}
\tag{28}
$$

$$A^n_{s,h}\left(\widehat{\boldsymbol{d}}^n_h, \widehat{\boldsymbol{w}}_h\right) = \rho_s \left(\frac{\zeta_0}{\Delta t^2}\widehat{\boldsymbol{d}}^n_h, \widehat{\boldsymbol{w}}_h\right)_{\widehat{\Omega}_s} + a_{s,h}\left(\widehat{\boldsymbol{d}}^n_h, \widehat{\boldsymbol{w}}_h\right); \tag{29}$$

$$\begin{aligned} A^n_{\Sigma,h}(\boldsymbol{u}^n_h, p^n_h, \boldsymbol{d}^n_h; \boldsymbol{v}_h, q_h, \boldsymbol{w}_h) = &-\left(\delta \boldsymbol{T}_f(\boldsymbol{u}^n_h, p^n_h)\boldsymbol{n} + (1-\delta)\boldsymbol{T}_s(\boldsymbol{d}^n_h)\boldsymbol{n}, \boldsymbol{v}_h - \boldsymbol{w}_h\right)_{\mathcal{F}^n_{\Sigma,h}} \\ &- \left(\boldsymbol{u}^n_h - \frac{\xi_0}{\Delta t}\boldsymbol{d}^n_h, \delta \boldsymbol{T}_f(\boldsymbol{v}_h, -q_h)\boldsymbol{n} + (1-\delta)\boldsymbol{T}_s(\boldsymbol{w}_h)\boldsymbol{n}\right)_{\mathcal{F}^n_{\Sigma,h}} \\ &+ \left(\sigma_\Sigma(\boldsymbol{u}^n_h - \frac{\xi_0}{\Delta t}\boldsymbol{d}^n_h), \boldsymbol{v}_h - \boldsymbol{w}_h\right)_{\mathcal{F}^n_{\Sigma,h}}; \end{aligned} \tag{30}$$

$$\begin{aligned} F^n_h(\boldsymbol{v}_h, \boldsymbol{w}_h) = &\rho\left(\sum_{i=1}^r \frac{\xi_i}{\Delta t}\boldsymbol{u}^{n-i}_h, \boldsymbol{v}_h\right)_{\Omega^n} + \rho_s\left(\sum_{i=1}^r \frac{\zeta_i}{\Delta t^2}\widehat{\boldsymbol{d}}^{n-i}_h, \widehat{\boldsymbol{w}}_h\right)_{\widehat{\Omega}_s} \\ &+ \left(\sum_{i=1}^r \frac{\xi_i}{\Delta t}\boldsymbol{d}^{n-i}_h, \delta \boldsymbol{T}_f(\boldsymbol{v}_h, -q_h)\boldsymbol{n} + (1-\delta)\boldsymbol{T}_s(\boldsymbol{w}_h)\boldsymbol{n}\right)_{\mathcal{F}^n_{\Sigma,h}} \\ &- \left(\sigma_\Sigma \sum_{i=1}^r \frac{\xi_i}{\Delta t}\boldsymbol{d}^{n-i}_h, \boldsymbol{v}_h - \boldsymbol{w}_h\right)_{\mathcal{F}^n_{\Sigma,h}} + (\boldsymbol{f}, \boldsymbol{v}_h)_{\Omega^n} + \left(\widehat{\boldsymbol{f}}_s, \widehat{\boldsymbol{w}}_h\right)_{\widehat{\Omega}_s}. \end{aligned} \tag{31}$$

The fully-discrete PolyDG approximation reads as follows: given $\delta \in [0,1]$, $\sigma_v \in L^\infty(\mathcal{F}^n_{f,h})$, $\sigma_p \in L^\infty(\mathcal{F}^n_{f,h})$, $\widehat{\sigma}_s \in L^\infty(\widehat{\mathcal{F}}_{s,h})$, $\sigma_\Sigma \in L^\infty(\mathcal{F}^n_{\Sigma,h})$, $\boldsymbol{f} \in [L^2(\Omega^n_f)]^2$ and $\widehat{\boldsymbol{f}}_s \in [L^2(\widehat{\Omega}_s)]^2$, for $n > 0$, find $(\boldsymbol{u}^n_h, p^n_h, \widehat{\boldsymbol{d}}^n_h) \in \boldsymbol{V}^{\ell,n}_h \times Q^{m,n}_h \times \boldsymbol{W}^\ell_h$, such that

$$A^n_{f,h}\left(\boldsymbol{u}^n_h, p^n_h; \boldsymbol{v}_h, q_h\right) + A^n_{s,h}\left(\widehat{\boldsymbol{d}}^n_h, \widehat{\boldsymbol{w}}_h\right) + A^n_{\Sigma,h}(\boldsymbol{u}^n_h, p^n_h, \boldsymbol{d}^n_h; \boldsymbol{v}_h, q_h, \boldsymbol{w}_h) = F^n_h(\boldsymbol{v}_h, \boldsymbol{w}_h),$$

for all $(\boldsymbol{v}_h, q_h, \widehat{\boldsymbol{w}}_h) \in \boldsymbol{V}^{\ell,n}_h \times Q^{m,n}_h \times \boldsymbol{W}^\ell_h$.

In (28), the pressure stabilization term $s^n_h : L^2_0 \times L^2_0 \to \mathbb{R}$ is that given in Section 2.1 evaluated on $\mathcal{F}^{n,i}_{f,h}$. In (29), we have introduced the bilinear forms $a^n_{f,h} : [H^1(\mathcal{T}^n_{f,h})]^d \times [H^1(\mathcal{T}^n_{f,h})]^d \to \mathbb{R}$, $b^n_h : L^2_0 \times [H^1(\mathcal{T}^n_{f,h})]^d \to \mathbb{R}$ and $a_{s,h} : [H^1(\widehat{\mathcal{T}}_{s,h})]^d \times [H^1(\widehat{\mathcal{T}}_{s,h})]^d \to \mathbb{R}$, which are defined as

$$\begin{aligned} a^n_{f,h}(\boldsymbol{u}^n_h, \boldsymbol{v}_h) = &\int_\Omega^n 2\mu \boldsymbol{D}_h(\boldsymbol{u}^n_h) : \nabla_h \boldsymbol{v}_h - \sum_{F \in \mathcal{F}^n_{f,h}} \int_F 2\mu\{\boldsymbol{D}_h(\boldsymbol{u}^n_h)\} : [\![\boldsymbol{v}_h]\!] \\ &- \sum_{F \in \mathcal{F}^n_{f,h}} \int_F 2\mu\, [\![\boldsymbol{u}^n_h]\!] : \{\boldsymbol{D}_h(\boldsymbol{v}_h)\} + \sum_{F \in \mathcal{F}^n_{f,h}} \int_F \sigma_v\, [\![\boldsymbol{u}_h]\!] : [\![\boldsymbol{v}_h]\!], \end{aligned}$$

$$b^n_h(p^n_h, \boldsymbol{v}^n_h) = -\int_\Omega^n p^n_h \nabla_h \cdot \boldsymbol{v}^n_h + \sum_{F \in \mathcal{F}^n_{f,h}} \int_F \{p^n_h \boldsymbol{I}\} : [\![\boldsymbol{v}^n_h]\!],$$

$$
\begin{aligned}
a_{s,h}(\widehat{\boldsymbol{d}}_h^n, \widehat{\boldsymbol{w}}_h) = & \int_{\widehat{\Omega}_s} 2\mu_s \boldsymbol{D}_h(\widehat{\boldsymbol{d}}_h^n) : \nabla_h \widehat{\boldsymbol{w}}_h + \int_{\widehat{\Omega}_s} \lambda_s \nabla_h \cdot \widehat{\boldsymbol{d}}_h^n \nabla_h \cdot \widehat{\boldsymbol{w}}_h \\
& - \sum_{F \in \widehat{\mathcal{F}}_{s,h}} \int_F 2\mu_s \{\boldsymbol{D}_h(\widehat{\boldsymbol{d}}_h^n)\} : [\![\widehat{\boldsymbol{w}}_h]\!] - \sum_{F \in \widehat{\mathcal{F}}_{s,h}} \int_F \lambda_s \{\nabla_h \cdot \widehat{\boldsymbol{d}}_h^n \boldsymbol{I}\} : [\![\widehat{\boldsymbol{w}}_h]\!] \\
& - \sum_{F \in \widehat{\mathcal{F}}_{s,h}} \int_F 2\mu_s \left[\!\!\left[\widehat{\boldsymbol{d}}_h^n\right]\!\!\right] : \{\boldsymbol{D}_h(\widehat{\boldsymbol{w}}_h)\} - \sum_{F \in \widehat{\mathcal{F}}_{s,h}} \int_F \lambda_s \left[\!\!\left[\widehat{\boldsymbol{d}}_h^n\right]\!\!\right] : \{\nabla_h \cdot \widehat{\boldsymbol{w}}_h \boldsymbol{I}\} \\
& + \sum_{F \in \widehat{\mathcal{F}}_{s,h}} \int_F \widehat{\sigma}_s \left[\!\!\left[\widehat{\boldsymbol{d}}_h^n\right]\!\!\right] : [\![\widehat{\boldsymbol{w}}_h]\!] \,,
\end{aligned}
$$

where $\boldsymbol{D}_h(\boldsymbol{w}) = 1/2(\nabla_h \boldsymbol{w} + \nabla_h^T \boldsymbol{w})$.

The functions σ_v and σ_p are given in Definition 2.1 on $\mathcal{F}_{f,h}^n$, while $\widehat{\sigma}_s : \mathcal{F}_{s,h}^n \to \mathbb{R}$ and $\sigma_\Sigma : \mathcal{F}_{\Sigma,h}^n \to \mathbb{R}$ are defined as

$$
\widehat{\sigma}_s|_F = \begin{cases} \gamma_s \max\limits_{K^+,K^-} \left\{ \dfrac{\ell^2 \overline{\mathcal{C}}_{s,K}}{h_K} \right\} & F \in \mathcal{F}_{s,h}^{n,i}, \\ \gamma_s \dfrac{\ell^2 \overline{\mathcal{C}}_{s,K}}{h_K} & F \in \mathcal{F}_{s,h}^{n,b}, \end{cases}
$$

$$
\sigma_\Sigma|_F = \gamma_\Sigma \max_{K^+,K^-} \left\{ \frac{\ell^2}{h_K} \left(\delta\mu + (1-\delta)\overline{\mathcal{C}}_{s,K} \right) \right\} \quad F \in \mathcal{F}_{\Sigma,h}^n,
$$

with γ_s, γ_Σ positive constants, $\overline{\mathcal{C}}_{s,K} = \|\mathcal{C}_s|K\|_{l^2}$ and $\mathcal{C}_{s,K}$ the linear elasticity fourth order tensor.

The fluid domain Ω^n and the interface Σ^n in (28), (30), and (31) are unknown. Thus, they are approximated with extrapolations of order r of the domains at the previous time steps.

Remark 6.1 *For the numerical stability of the FSI problem, theoretical results show that the parameter δ appearing in the interface terms of equation (30) and (31) has to be set equal to 1; see [7].*

7 Numerical results

In this section, we present some numerical experiments for the steady Stokes problem and the time-dependent FSI problem. In Section 7.1, we assess the order of accuracy of the method for the steady Stokes problem as the spatial discretization parameter tends to zero and the spatial polynomial degree increases. In Section 7.2, we consider a FSI problem and we numerically compare the pressure field for different choices of the velocity and pressure spaces, with and without the pressure stabilization term. Finally, in Section 7.3, we show that the proposed PolyDG method is able to reproduce the expected dynamics of a time-dependent FSI problem.

For all the proposed examples, the resulting linear system corresponding to the Stokes and the FSI problems is solved in Matlab by means of a direct method.

7.1 The steady Stokes problem: convergence results

Here, we numerically estimate the order of convergence of the steady Stokes problem with respect to the spatial parameter h when it tends to zero and the spatial polynomial degree increases.

We consider a square unit domain $\Omega = [0,1]^2$ and the exact solution

$$\boldsymbol{u}_{ex} = \begin{bmatrix} -cos(2\pi x)sin(2\pi y) \\ \\ sin(2\pi x)cos(2\pi y) \end{bmatrix}, \qquad p_{ex} = 1 - e^{-x(x-1)(x-0.5)^2 - y(y-1)(y-0.5)^2}.$$

The forcing term $\boldsymbol{f}$ and the Dirichlet boundary conditions are computed accordingly. We picked $\boldsymbol{u}_{ex}$ so that $\nabla \cdot \boldsymbol{u}_{ex} = 0$. We set $\mu = 1$, $\gamma_v = 10$, $\gamma_p = 10$ and $m = \ell = 4$. In Figure 9 (left), we plot the error in the L^2 and DG-norms of the velocity, in the L^2-norm of the pressure and in the pressure semi-norm $|\cdot|_{\mathsf{J}}$ versus $h\frac{1}{\sqrt{N_{el}}}$. The expected order of convergence are found. In Figure 9 (right), we show the errors with respect to the polynomial degree m, with an underlying uniform and regular polygonal mesh, generated via `PolyMesher` [53], consisting of $N_{el} = 160$ elements. We observe exponential convergence in terms of the polynomial degree.

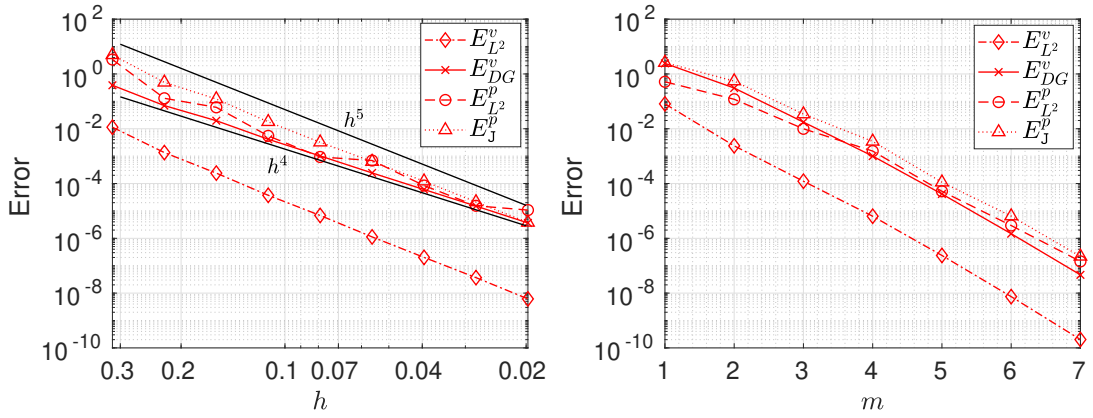

Figure 9: Numerical estimates of the order of convergence with respect to the mesh size h (left) and the polynomial degree m (right).

Remark 7.1 *Within the theoretical setting of the paper, we cannot prove the exponential convergence of the p-version of the method. Notwithstanding, it is the expected behaviour in the standard Galerkin setting with simplicial and tensor product element meshes for*

analytic solutions; see, e.g., [50] and the references therein. The reason of this resides in the continuity property of the Stein extension operator (10), which is valid modulo a hidden constant depending on the involved Sobolev regularity s. In particular, when trying to recover exponential convergence, a term growing more than exponentially with respect to s appears.

A possible way to overcome this issue would be to resort to a different approach, where we assume that the solution is analytic over a slightly larger domain than Ω. In particular, we should substitute the approximation result in Lemma 3.2 with some approximation properties by means of tensor product Legendre polynomials on tensor product element and Koornwinder polynomials on simplicial elements; see, e.g., [50] and [18] for more details, respectively. We avoid further details on this point, for it might render the understanding of the paper more cumbersome.

The suboptimality in terms of the polynomial degree due to the nonrobustness of the inf-sup condition, see Remark 5.1, is eaten up by the expected exponential convergence for analytic solutions.

7.2 The fluid-structure interaction problem: numerical comparison of the pressure fields

In this first numerical test we compare the pressure field for different choices of the spatial polynomial degree of the discrete velocity and pressure spaces for a FSI problem. The fluid domain Ω represents a viscous fluid with density $\rho = 1\,\mathrm{g/cm^2}$ and viscosity $\mu = 0.03\,\mathrm{g/s}$, while the structure domain Ω_s is a linear elastic barrier that horizontally divides the fluid domain in two compartments; see Figure 10. For the structure we set the density $\rho_s = 1.2\,\mathrm{g/cm^2}$, the Young's modulus $E = 2{\cdot}10^4\,\mathrm{dyne/cm}$, and the Poisson's ratio $\nu = 0.49$.

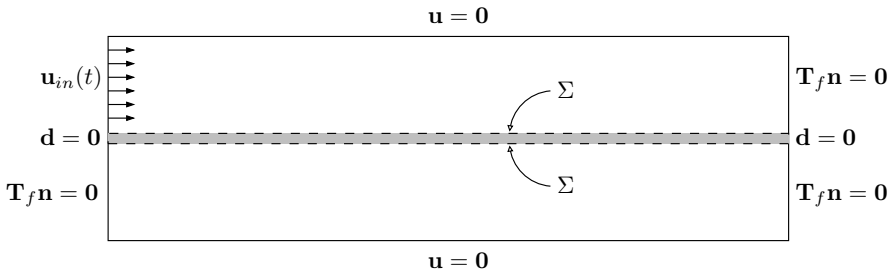

Figure 10: Setting of the boundary conditions on the fluid (white) and structure (grey) domains. The moving fluid-structure interface is depicted by dashed lines.

At the upper and lower boundaries of the fluid domain, we impose zero velocity, i.e., $\boldsymbol{u} = \mathbf{0}$, and the barrier is fixed on the left and right sides, i.e., $\boldsymbol{d} = \mathbf{0}$. To the system, initially at rest, is prescribed an inlet velocity $\boldsymbol{u}_{in}(t) = (u_{in,x}(t), 0)\,\mathrm{cm/s}$ to the upper

compartment from the left boundary, where

$$u_{in,x}(t) = \begin{cases} 10t & t \leq 0.1, \\ 0 & \text{otherwise}, \end{cases}$$

while we prescribe a homogeneous Neumann condition to the other three ends of the two compartments. The fluid-structure interface Σ, namely the upper and lower boundaries of the barrier, is free to move; see Figure 10.

In the discrete setting, we set $\Delta t = 10^{-3}$ s, $T = 0.25$ s, $\gamma_v = \gamma_p = 10$ and $\delta = 1$; see Remark 6.1. The fluid and structure meshes initially consist of uniform and regular triangles consisting of 1100 elements ($h = 0.025$ cm) and 400 elements ($h = 0.01$ cm), respectively. Due to their intersection, polygonal elements appear. We employ the Backward Difference Formula (BDF) scheme of order 3 for the temporal discretization.

We pick the pairs of velocity and pressure spaces $\mathcal{P}^\ell - \mathcal{P}^m$, with $\ell = 3$ and $m = 1, 2, 3$, both with and without the pressure stabilization term (4d). The spatial polynomial order of discrete displacement field is set equal to $\ell = 3$.

In Figure 11, we plot the pressure field at time $t = 0.1$ s for all the considered configurations. As expected, for a fixed pair of spaces $\mathcal{P}^3 - \mathcal{P}^m$, $m = 1, 2, 3$, the stabilized pair yields a stable and more regular pressure field compared to the not stabilized one. The not stabilized $\mathcal{P}^3 - \mathcal{P}^3$ pair, Figure 11b, leads to an oscillating pressure field near the inlet boundary and all along the fluid-structure interface, where elements of general shape appear. This instabilities become less evident as the pressure polynomial order decreases; see Figure 11d and Figure 11f. On the other hand, the stabilized $\mathcal{P}^3 - \mathcal{P}^3$ pair, Figure 11a, shows some oscillations only at the corners of the inlet boundary, where we expect a lower regularity in the solution, a pressure peak and strong pressure gradients. For the stabilized $\mathcal{P}^3 - \mathcal{P}^2$ and $\mathcal{P}^3 - \mathcal{P}^1$ cases, see Figure 11c and Figure 11e, the pressure field does not present any noticeable oscillation. Moreover, there is no significant difference in the fluid velocity and structure displacement fields.

7.3 The fluid-structure interaction problem: an elastic membrane in a pipe

Here, we consider a second fluid-structure interaction problem aiming at showing that the proposed PolyDG discretization method is able to reproduce the expected dynamics of the system with a stable pressure field. More precisely, we consider a pipe filled by a viscous fluid with an immersed linear elastic membrane that blocks the flow. The pipe is represented by a fluid domain Ω of size $0.4\,\text{cm} \times 0.2\,\text{cm}$, while the solid domain Ω_s represents the elastic membrane of size $0.01\,\text{cm} \times 0.2\,\text{cm}$ centred in the pipe; see Figure 12. At initial time, the system is at rest. The membrane is clamped at the pipe, i.e., $\boldsymbol{d} = \boldsymbol{0}$ on the upper and lower sides of Ω_s. At the top and bottom boundaries of the fluid domain, $\boldsymbol{u} = \boldsymbol{0}$, while on the left and right sides we prescribe a jump in the stress, namely, $\boldsymbol{\sigma}_f \boldsymbol{n} = (-10, 0)\,\text{dyne/cm}$ and $\boldsymbol{\sigma}_f \boldsymbol{n} = \boldsymbol{0}$, respectively. This induces oscillations in

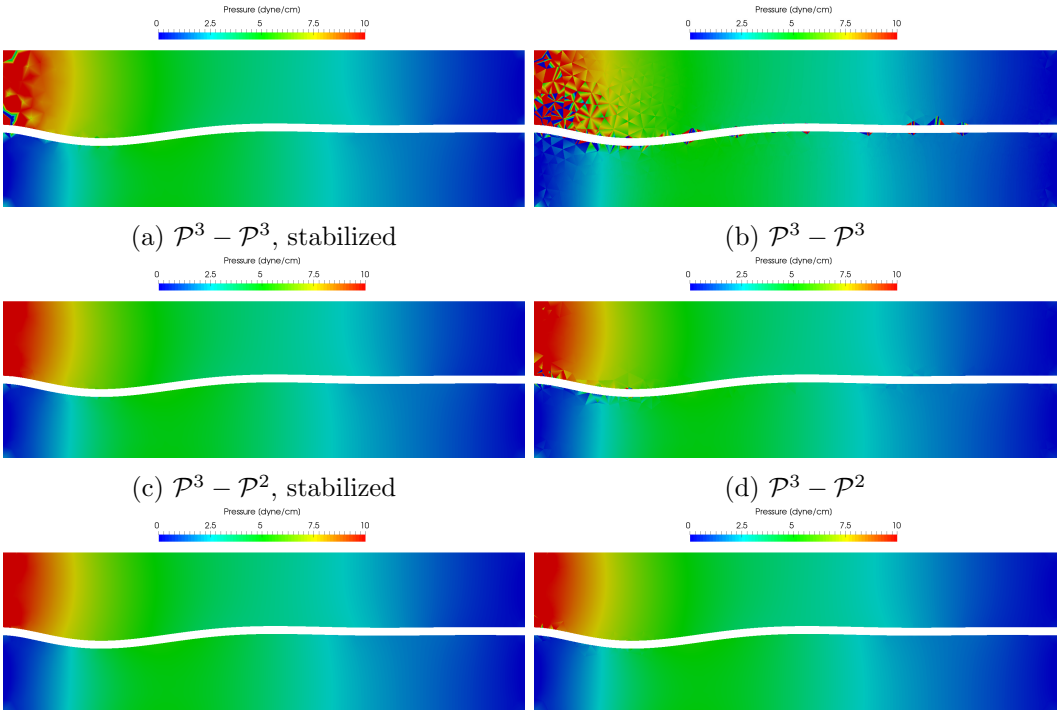

(a) $\mathcal{P}^3 - \mathcal{P}^3$, stabilized

(b) $\mathcal{P}^3 - \mathcal{P}^3$

(c) $\mathcal{P}^3 - \mathcal{P}^2$, stabilized

(d) $\mathcal{P}^3 - \mathcal{P}^2$

(e) $\mathcal{P}^3 - \mathcal{P}^1$, stabilized

(f) $\mathcal{P}^3 - \mathcal{P}^1$

Figure 11: Pressure field at time $t = 0.1\,\mathrm{s}$ for different choices of the pressure space $\mathcal{P}^m$, $m = 1, 2, 3$, with pressure stabilization (left) and without stabilization (right). The velocity space is fixed to $\mathcal{P}^3$.

the structure, which are subsequently dumped by the viscous fluid until a steady state is reached. At the steady state, we expect a uniform pressure inside each chamber of the pipe. The fluid and structure have the following material properties: $\rho = \rho_s = 1\,\mathrm{g/cm^2}$, $\mu = 0.1\,\mathrm{g/s}$, $E = 10^4\,\mathrm{dyne/cm}$ and $\nu = 0.45$.

For the numerical simulation, we consider a fluid mesh consisting of 1400 elements ($h = 0.0125\,\mathrm{cm}$) and a solid mesh consisting of 400 elements ($h = 0.004\,\mathrm{cm}$); see Figure 12. Although the meshes are initially made of regular triangles, their intersection generates elements of general shape. We consider the following discrete parameters: $\Delta t = 0.002\,\mathrm{s}$, $\gamma_v = \gamma_p = 10$, $\delta = 1$, see Remark 6.1, and $\ell = 3$, $m = 2$ with pressure stabilization. For the time discretization, we employ the 3-rd order BDF scheme.

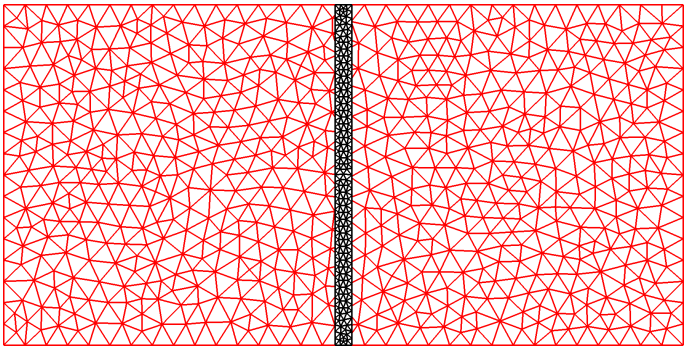

Figure 12: "Pipe" test case. Fluid (red) and structure (black) meshes.

In Figure 13 (left), we show the configuration at the steady state, $t = 1\,s$. As expected, each of the two chambers of the pipe reach a uniform value of the pressure. In Figure 13 (right), we plot the x-displacement of the structure at its center of mass.

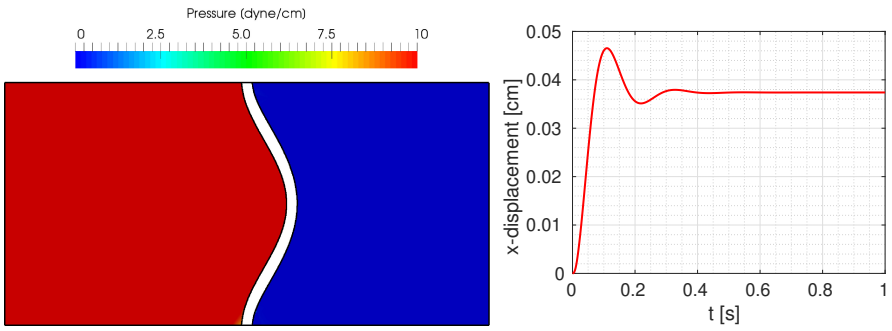

Figure 13: "Pipe" test case. Left: pressure field and position of the structure at the steady state ($t = 1\,\mathrm{s}$). Right: evolution in time of the x-displacement of the structure at the center of mass.

8 Conclusions

In this work, we showed the well-posedness of the discrete Stokes problem obtained via a Discontinuous Galerkin approximation for polygonal and polyhedral grids. In particular, we proved a generalized *inf-sup* condition that is valid for $m - \ell \leq 1$, with ℓ and m the spatial polynomial degrees for the velocity and pressure spaces, respectively. Under suitable mesh assumptions, we proved that the discrete *inf-sup* constant is uniform with respect to the mesh size and presents a mild dependence with respect to the spatial polynomial degree. Moreover, from the numerical tests, the discrete *inf-sup* constant seems to be independent of the size of the edges in much more general configurations than those addressed theoretically, indicating that the method is robust with respect to degenerating edges. We also proved a priori error estimate in the energy norm for the Stokes problem that is suboptimal with respect to the polynomial degree, since it inherits the suboptimality of the discrete *inf-sup* constant. Finally, we presented numerical examples by considering a time-dependent fluid-structure interaction problem in the case of large displacement regime showing that the proposed PolyDG method is able to produce stable solutions.

Acknowledgments

PFA, LM, MV and SZ are member of the INdAM Research group GNCS and this work is partially funded by INDAM-GNCS. PFA, MV and SZ have been partially funded by the PRIN Italian research grant n. 201744KLJL funded by MIUR.

References

[1] C. Ager, B. Schott, A.-T. Vuong, A. Popp, and W. A. Wall. A consistent approach for fluid-structure-contact interaction based on a porous flow model for rough surface contact. *Internat. J. Numer. Methods Engrg.*, 2019.

[2] F. Alauzet, B. Fabrèges, M. A. Fernández, and M. Landajuela. Nitsche-XFEM for the coupling of an incompressible fluid with immersed thin-walled structures. *Comput. Methods Appl. Mech. Engrg.*, 301:300–335, 2016.

[3] P. F. Antonietti, A. Cangiani, J. Collis, Z. Dong, E. H. Georgoulis, S. Giani, and P. Houston. Review of Discontinuous Galerkin Finite Element Methods for Partial Differential Equations on Complicated Domains. In *Building Bridges: Connections and Challenges in Modern Approaches to Numerical Partial Differential Equations*, pages 281–310. Springer, 2016.

[4] P. F. Antonietti, C. Facciolá, P. Houston, I. Mazzieri, G. Pennesi, and M. Verani. High-Order Discontinuous Galerkin Methods on Polyhedral Grids for Geophysical Applications: Seismic Wave Propagation and Fractured Reservoir Simulations. In *SEMA-SIMAI Springer series on Polyhedral Methods in Geosciences*. Springer, 2020.

[5] P. F. Antonietti, S. Giani, and P. Houston. *hp*-version composite Discontinuous Galerkin methods for elliptic problems on complicated domains. *SIAM J. Sci. Comput.*, 35(3):A1417–A1439, 2013.

[6] P. F. Antonietti and I. Mazzieri. High-order Discontinuous Galerkin methods for the elastodynamics problem on polygonal and polyhedral meshes. *Comput. Methods Appl. Mech. Engrg.*, 342:414–437, 2018.

[7] P. F. Antonietti, M. Verani, C. Vergara, and S. Zonca. Numerical solution of fluid-structure interaction problems by means of a high order Discontinuous Galerkin method on polygonal grids. *Finite Elem. Anal. Des.*, 159:1–14, 2019.

[8] I. Babuška and M. Suri. The *h-p* version of the finite element method with quasi-uniform meshes. *ESAIM Math. Model. Numer. Anal.*, 21(2):199–238, 1987.

[9] I. Babuška and M. Suri. The optimal convergence rate of the *p*-version of the finite element method. *SIAM J. Numer. Anal.*, 24(4):750–776, 1987.

[10] F. Bassi, L. Botti, A. Colombo, D. A. Di Pietro, and P. Tesini. On the flexibility of agglomeration based physical space discontinuous Galerkin discretizations. *J. Comput. Phys.*, 231(1):45–65, 2012.

[11] L. Beirão Da Veiga, C. Canuto, R. H. Nochetto, and G. Vacca. Equilibrium analysis of an immersed rigid leaflet by the virtual element method. *arXiv preprint arXiv:2007.09130*, 2020.

[12] L. Beirão da Veiga, C. Lovadina, and G. Vacca. Divergence free virtual elements for the Stokes problem on polygonal meshes. *ESAIM Math. Model. Numer. Anal.*, 51(2):509–535, 2017.

[13] D. Boffi, F. Brezzi, and M. Fortin. *Mixed Finite Element Methods and Applications*, volume 44. Springer Series in Computational Mathematics, 2013.

[14] D. Boffi and L. Gastaldi. A fictitious domain approach with Lagrange multiplier for fluid-structure interactions. *Numer. Math.*, 135(3):711–732, 2017.

[15] I. Borazjani. Fluid–structure interaction, immersed boundary-finite element method simulations of bio-prosthetic heart valves. *Comput. Methods Appl. Mech. Engrg.*, 257:103–116, 2013.

[16] R. Borker, D. Huang, S. Grimberg, C. Farhat, P. Avery, and J. Rabinovitch. Mesh adaptation framework for embedded boundary methods for computational fluid dynamics and fluid-structure interaction. *Internat. J. Numer. Methods Fluids*, 90(8):389–424, 2019.

[17] N. Bouaanani and S. Renaud. Effects of fluid–structure interaction modeling assumptions on seismic floor acceleration demands within gravity dams. *Eng. Struct.*, 67:1–18, 2014.

[18] D. Braess and Ch. Schwab. Approximation on simplices with respect to weighted Sobolev norms. *J. Approx. Theory*, 103(2):329–337, 2000.

[19] F. Brezzi. On the existence, uniqueness and approximation of saddle-point problems arising from Lagrangian multipliers. *Publications mathématiques et informatique de Rennes*, S4:1–26, 1974.

[20] E. Burman, M. A. Fernández, and S. Frei. A Nitsche-based formulation for fluid-structure interactions with contact. *ESAIM Math. Model. Numer. Anal.*, 54(2):531–564, 2020.

[21] A. Cangiani, Z. Dong, and E. H. Georgoulis. *hp*-version space-time discontinuous Galerkin methods for parabolic problems on prismatic meshes. *SIAM J. Sci. Comput.*, 39(4):A1251–A1279, 2017.

[22] A. Cangiani, Z. Dong, and E. H. Georgoulis. *hp*-version discontinuous Galerkin methods on essentially arbitrarily-shaped elements, 2019.

[23] A. Cangiani, Z. Dong, E. H. Georgoulis, and P. Houston. *hp*-Version discontinuous Galerkin methods for advection-diffusion-reaction problems on polytopic meshes. *ESAIM Math. Model. Numer. Anal.*, 50(3):699–725, 2016.

[24] A. Cangiani, Z. Dong, E. H. Georgoulis, and P. Houston. *hp-Version Discontinuous Galerkin Methods on Polygonal and Polyhedral Meshes*. Springer, 2017.

[25] A. Cangiani, E. H. Georgoulis, and P. Houston. *hp*-version discontinuous Galerkin methods on polygonal and polyhedral meshes. *Math. Models Methods Appl. Sci.*, 24(10):2009–2041, 2014.

[26] B. Cockburn, G. Kanschat, D. Schötzau, and C. Schwab. Local discontinuous Galerkin methods for the Stokes system. *SIAM J. Numer. Anal.*, 40(1):319–343, 2002.

[27] S. Court and M. Fournié. A fictitious domain finite element method for simulations of fluidstructure interactions: The Navier-Stokes equations coupled with a moving solid. *J. Fluid. Struct.*, 55:398–408, 2015.

[28] D. A. Di Pietro and J. Droniou. *The Hybrid High-Order Method for Polytopal Meshes: Design, Analysis, and Applications*, volume 19 of *MS&A Modeling, Simulation and Applications*. Springer, 2020.

[29] D. A. Di Pietro and A. Ern. Discrete functional analysis tools for discontinuous Galerkin methods with application to the incompressible Navier-Stokes equations. *Math. Comp.*, 79(271):1303–1330, 2010.

[30] D. A. Di Pietro and A. Ern. *Mathematical aspects of discontinuous Galerkin methods*, volume 69 of *Mathématiques & Applications*. Springer, Heidelberg, 2012.

[31] J. Donea. An arbitrary Lagrangian-Eulerian finite element method for transient dynamic fluid-structure interaction. *Comput. Methods Appl. Mech. Engrg.*, 33:689–723, 1982.

[32] M. Dumbser, F. Fambri, I. Furci, M. Mazza, S. Serra-Capizzano, and M. Tavelli. Staggered discontinuous Galerkin methods for the incompressible Navier–Stokes equations: Spectral analysis and computational results. *Numerical Linear Algebra with Applications*, 25(5):e2151, 2018.

[33] H. C. Elman, D. J. Silvester, and A. J. Wathen. *Finite Elements and Fast Iterative Solvers: with applications in incompressible fluid dynamics*. Oxford University Press, USA, 2014.

[34] M. Fedele, E. Faggiano, L. Dede, and A. Quarteroni. A patient-specific aortic valve model based on moving resistive immersed implicit surfaces. *Biomech. Model. Mechan.*, 16(5):1779–1803, 2017.

[35] A. Gerstenberger and W. A. Wall. An extended finite element method/Lagrange multiplier based approach for fluid–structure interaction. *Comput. Methods Appl. Mech. Engrg.*, 197(19):1699–1714, 2008.

[36] R. P. Ghosh, G. Marom, M. Bianchi, K. D'souza, W. Zietak, and D. Bluestein. Numerical evaluation of transcatheter aortic valve performance during heart beating and its post-deployment fluid–structure interaction analysis. *Biomech. Model. in Mechan.*, pages 1–16, 2020.

[37] V. Girault, B. Rivière, and M. Wheeler. A discontinuous Galerkin method with nonoverlapping domain decomposition for the Stokes and Navier-Stokes problems. *Math. Comp.*, 74(249):53–84, 2005.

[38] R. Glowinski, T.-W. Pan, T. I. Hesla, D. D. Joseph, and J. Periaux. A fictitious domain approach to the direct numerical simulation of incompressible viscous flow past moving rigid bodies: application to particulate flow. *J. Comput. Phys.*, 169(2):363–426, 2001.

[39] B. E. Griffith. Immersed boundary model of aortic heart valve dynamics with physiological driving and loading conditions. *Int. J. Numer. Methods Biomed. Eng.*, 28(3):317–345, 2012.

[40] E. Hairer, S. P. Nørsett, and G. Wanner. *Solving Ordinary Differential Equations I. Nonstiff Problems*. Springer-Verlag Berlin Heidelberg, 1993.

[41] P. Hansbo and M. G. Larson. Discontinuous Galerkin methods for incompressible and nearly incompressible elasticity by Nitsche's method. *Comput. Methods Appl. Mech. Engrg.*, 191(17-18):1895–1908, 2002.

[42] J. Hron and S. Turek. A monolithic FEM/multigrid solver for an ALE formulation of fluid-structure interaction with applications in biomechanics. In *Fluid-structure interaction*, pages 146–170. Springer, 2006.

[43] R. Kamakoti and W. Shyy. Fluid–structure interaction for aeroelastic applications. *Progress in Aerospace Sciences*, 40(8):535–558, 2004.

[44] A. Massing, M. G. Larson, A. Logg, and M. E. Rognes. A Nitsche-based cut finite element method for a fluid-structure interaction problem. *Commun. Appl. Math. Comput. Sci.*, 10(2):97–120, 2015.

[45] R. Mittal and G. Iaccarino. Immersed boundary methods. *Annu. Rev. Fluid Mech.*, 37(1):239–261, 2005.

[46] R. Picelli, S. Ranjbarzadeh, R. Sivapuram, R.S. Gioria, and E.C.N. Silva. Topology optimization of binary structures under design-dependent fluid-structure interaction loads. *Struct. Multidiscip. Optim.*, pages 1–16, 2020.

[47] D. Schötzau, C. Schwab, and R. Stenberg. Mixed *hp*-FEM on anisotropic meshes II: Hanging nodes and tensor products of boundary layer meshes. *Numer. Math.*, 83(4):667–697, 1999.

[48] D. Schötzau, C. Schwab, and A. Toselli. Mixed *hp*-DGFEM for incompressible flows. *SIAM J. Numer. Anal.*, 40(6):2171–2194, 2002.

[49] D. Schötzau, C. Schwab, and A. Toselli. Stabilized *hp*-DGFEM for incompressible flow. *Math. Models Methods Appl. Sci.*, 13(10):1413–1436, 2003.

[50] Ch. Schwab. *p- and hp- Finite Element Methods: Theory and Applications in Solid and Fluid Mechanics*. Clarendon Press Oxford, 1998.

[51] E. M. Stein. *Singular Integrals and Differentiability Properties of Functions*. Princeton University Press, Princeton, NY, 1970.

[52] R. Stenberg and M. Suri. Mixed *hp* finite element methods for problems in elasticity and Stokes flow. *Numer. Math.*, 72(3):367–389, 1996.

[53] C. Talischi, G. H. Paulino, A. Pereira, and I. F. M. Menezes. Polymesher: a general-purpose mesh generator for polygonal elements written in Matlab. *Struct. Multidiscip. Optim.*, 45(3):309–328, 2012.

[54] M. Tavelli and M. Dumbser. Arbitrary high order accurate space–time discontinuous Galerkin finite element schemes on staggered unstructured meshes for linear elasticity. *Journal of Computational Physics*, 366:386–414, 2018.

[55] A. Tello, R. Codina, and J. Baiges. Fluid structure interaction by means of variational multiscale reduced order models. *Internat. J. Numer. Methods Engrg.*, 121(12):2601–2625, 2020.

[56] T. Terahara, K. Takizawa, T. E. Tezduyar, Y. Bazilevs, and M.-C. Hsu. Heart valve isogeometric sequentially-coupled FSI analysis with the space–time topology change method. *Comput. Mech.*, pages 1–21, 2020.

[57] T. E. Tezduyar and S. Sathe. Modelling of fluid–structure interactions with the space–time finite elements: Solution techniques. *Internat. J. Numer. Methods Fluids*, 54(6-8):855–900, 2007.

[58] A. Toselli. *hp* discontinuous Galerkin approximations for the Stokes problem. *Math. Models Methods Appl. Sci.*, 12(11):1565–1597, 2002.

[59] A. Toselli and C. Schwab. Mixed *hp*-finite element approximations on geometric edge and boundary layer meshes in three dimensions. *Numer. Math.*, 94(4):771–801, 2003.

[60] D. Wiresaet, E. J. Kubatko, C. E. Michoski, S. Tanaka, J. J. Westerink, and C. Dawson. Discontinuous Galerkin methods with nodal and hybrid modal/nodal triangular, quadrilateral, and polygonal elements for nonlinear shallow water flow. *Comput. Methods Appl. Mech. Engrg.*, 270:113–149, 2014.

[61] D. Xu, E. Kaliviotis, A. Munjiza, E. Avital, C. Ji, and J. Williams. Large scale simulation of red blood cell aggregation in shear flows. *J. Biomech.*, 46(11):1810–1817, 2013.

[62] L. T. Zhang and M. Gay. Immersed finite element method for fluid-structure interactions. *J. Fluid. Struct.*, 23(6):839–857, 2007.

MOX Technical Reports, last issues

Dipartimento di Matematica
Politecnico di Milano, Via Bonardi 9 - 20133 Milano (Italy)

80/2020 Zingaro, A.; Dede', L.; Menghini, F.; Quarteroni, A.
Hemodynamics of the heart's left atrium based on a Variational Multiscale-LES numerical model

78/2020 Regazzoni, F.; Salvador, M.; Africa, P.c.; Fedele, M.; Dede', L.; Quarteroni, A.
A cardiac electromechanics model coupled with a lumped parameters model for closed-loop blood circulation. Part II: numerical approximation

79/2020 Regazzoni, F.; Salvador, M.; Africa, P.c.; Fedele, M.; Dede', L.; Quarteroni, A.
A cardiac electromechanics model coupled with a lumped parameters model for closed-loop blood circulation. Part I: model derivation

77/2020 Parolini, N.; Ardenghi, G.;Dede’, L.; Quarteroni, A.
A Mathematical Dashboard for the Analysis of Italian COVID-19 Epidemic Data

75/2020 F. Dassi; A. Fumagalli; D. Losapio; S. Scialò; A. Scotti; G. Vacca
The mixed virtual element method for grids with curved interfaces

76/2020 Centofanti, F.; Lepore, A.; Menafoglio, A.; Palumbo, B.; Vantini, S.
Functional Regression Control Chart

74/2020 Formaggia, L; Fumagalli, A.; Scotti, A.
A multi-layer reactive transport model for fractured porous media

67/2020 Caramenti, L.; Menafoglio, A.; Sgobba, S.; Lanzano, G.
Multi-Source Geographically Weighted Regression for Regionalized Ground-Motion Models

69/2020 Galvani, M.; Torti, A.; Menafoglio, A.; Vantini S.
FunCC: a new bi-clustering algorithm for functional data with misalignment

70/2020 Belli E.
Smoothly Adaptively Centered Ridge Estimator